

# Comparative fracture prediction study for two materials under a wide range of stress states using seven uncoupled models

Mariem Nouira<sup>a,b,c,\*</sup>, Marta Cristina Oliveira<sup>b</sup>, Ali Khalfallah<sup>a,b,d</sup>, José Luís Alves<sup>e</sup>,  
Luís Filipe Menezes<sup>b</sup>

<sup>a</sup> Laboratoire de Génie Mécanique, Ecole Nationale d'Ingénieurs de Monastir, Université de Monastir, Av. Ibn ElJazzar, 5019 Monastir, Tunisia

<sup>b</sup> CEMMPRE, Department of Mechanical Engineering, University of Coimbra, Polo II, Pinhal de Marrocos, 3030-788 Coimbra, Portugal

<sup>c</sup> Ecole Nationale d'Ingénieurs de Sousse, Université de Sousse, 4003 Sousse, Tunisia

<sup>d</sup> DGM, Institut Supérieur des Sciences Appliquées et de Technologie de Sousse, Cite Ibn Khaldoun 4003-Sousse, Université de Sousse, Tunisia

<sup>e</sup> CMEMS, Department of Mechanical Engineering, University of Minho, Campus de Azurém, 4800-058 Guimarães, Portugal

## ARTICLE INFO

### Keywords:

Ductile fracture  
Uncoupled model  
Calibration procedure  
Number of tests  
Type of tests

## ABSTRACT

The prediction of ductile failure is crucial for the progress of metal forming industries. Therefore, uncoupled fracture models have been proposed and continuously extended, trying to improve their forecasting abilities. However, without an assessment analysis of their predictive ability, it is difficult to establish the most suitable model, for describing the onset of failure under a wide range of loading conditions. Actually, a fair comparison of models' predictive ability requires the use of an extensive experimental database and a similar calibration procedure. In this context, seven uncoupled fracture models are chosen and revisited to study the effect of the type and number of tests used for calibration on their predictive ability. Experimental datasets available in literature were considered for 2024-T351 aluminium alloy and for DP600 steel. For each material, the experimental dataset was split in two subsets. The first one includes tests that were carried out under plane stress conditions that were used in the calibration procedure. For the aluminium alloy, different groups of 6 tests, covering distinct stress states, were elicited from the experimental subset and applied in the calibration of the seven models. The remaining tests were used to assess the predictive ability and their sensibility regarding the group used in models' calibration. Different trends of the fracture loci are observed, depending on the selected models and the tests used in their calibration. However, the analysis of the results indicates that a set of at least 6 experimental tests is appropriate to calibrate fracture models, providing that they enable covering a wide range for the stress triaxiality and Lode parameter. Finally, the conclusions provide some recommendations for the improvement of the calibration procedure.

## 1. Introduction

Thanks to the advent of digital computer capacities, numerical simulation codes have become fundamental tools in the development of metal forming processes, due to their ability to predict the material behaviour and occurrence of defects. However, the modelling of the ductile fracture is still a major challenge for the failure prediction during metal forming processes. Various approaches

\* Corresponding author at: Laboratoire de Génie Mécanique, Ecole Nationale d'Ingénieurs de Monastir, Université de Monastir, Av. Ibn ElJazzar, 5019 Monastir, Tunisia.

E-mail address: [mariem.nouira@student.dem.uc.pt](mailto:mariem.nouira@student.dem.uc.pt) (M. Nouira).

<https://doi.org/10.1016/j.engfracmech.2022.108952>

Received 28 August 2022; Received in revised form 6 November 2022; Accepted 16 November 2022

Available online 30 December 2022

0013-7944/© 2022 Elsevier Ltd. All rights reserved.

## Nomenclature

$\bar{\epsilon}^p$	Equivalent plastic strain
$\bar{\epsilon}_f$	Equivalent strain to fracture
$\bar{\epsilon}_{f,t}$	Equivalent strain to fracture under uniaxial tension
$\bar{\epsilon}_{f,s}$	Equivalent strain to fracture under pure shear
$\bar{\epsilon}_f^{(-)}$	Equivalent strain to fracture under normalized uniaxial compression
$\bar{\epsilon}_f^{(0)}$	Equivalent strain to fracture under normalized plane strain
$\bar{\epsilon}_f^{(+)}$	Equivalent strain to fracture under normalized uniaxial tension
$\bar{\epsilon}_{f, \text{Predicted}, i}$	Predicted fracture strain for the test $i$
$\bar{\epsilon}_{f, \text{Experimental}, i}$	Experimental fracture strain for the test $i$
$\theta$	Lode angle
$\bar{\theta}$	Normalized Lode angle
$\xi$	Normalized third invariant of the deviatoric stress tensor
$\sigma$	Cauchy stress tensor
$\sigma_m$	Mean stress or hydrostatic stress
$\sigma_n$	Normal stress
$\sigma_1, \sigma_2, \sigma_3$	Principal components of the Cauchy stress tensor
$\bar{\sigma}$	von Mises equivalent stress
$\bar{\sigma}_f$	Equivalent stress to fracture
$\bar{\sigma}_{HF}$	Hosford equivalent stress
$\tau$	Shear stress
$\tau_{\max}$	Maximum shear stress
$\eta$	Stress triaxiality
$(\psi_1, \dots, \psi_n)$	Material parameters
$A, n$	Hardening law parameters
$a, b, c$	Fracture parameters' for the H-C model
$c_1, c_2, c_3$	Fracture parameters' for the MMC model
$c_1, c_2, c_3$	Fracture parameters' for the L-H model
$C_1, C_2, C_3, C_4, m$	Fracture parameters' for the X-W model
$C_1, C_2, C_3$	Fracture parameters' for the Q-K model
$C$	Height of cut-off value of stress triaxiality for L-H model
$c_{\theta}^{\text{ax}}, c_{\theta}^c, c_{\theta}^s$	MMC fracture parameters' that controls the dependence of the Lode angle parameter and the asymmetry of fracture locus, respectively
$D$	Damage indicator
$D_1, D_2, D_3, D_4$	Fracture parameters' for the M-W model
$D_1, D_2, D_3, D_4, D_5, D_6$	Fracture parameters' for the B-W model
$Err$	Relative error function
$f_1, f_2, f_3$	Lode angle parameter functions presented in H-C model
$f(\eta, L)$	Dependency function on Lode parameter for the L-H model
$g_1[\eta, L]$	Dependency function on stress triaxiality and Lode parameter for Q-K, 2020 model
$g_2[L]$	Dependency function on Lode parameter for Q-K model
$i$	Number of test
$J_2, J_3$	Second and third invariant of the deviatoric stress tensor
$L$	Lode parameter
$N$	Number of tests used for calibration
$s_1, s_2, s_3$	Deviatoric principal stresses
$s$	Deviatoric stress tensor
$\langle \rangle$	Macaulay brackets

have been adopted to improve the understanding of the mechanisms involved in ductile fracture, by combining experimental and mechanical testing ([1,2]); microscopic observations ([3,4,5]) and numerical analysis ([6,7]). Nowadays, it is consensual that the nucleation, growth and coalescence of micro-voids play the major role at the microscopic level, influencing shear band formation ([8,9,10,11]). Therefore, several damage models have been proposed based on these ductile fracture mechanisms, which are commonly classified into coupled and uncoupled models.

The first category of ductile fracture models comprises coupled models, where the damage accumulation is inherent to the constitutive model, i.e., the stress tensor is coupled with the damage variable that affects the dissipation potential of the plastic deformation. The most widely known coupled ductile fracture model is the one commonly referred as Gurson-Tvergaard and

Needleman (GTN) [12]. It is based on the Gurson's model [13], which assumes the damaged material as a porous media (porous plasticity theory) and, consequently, introduces the concept of void volume fraction. However, the void growth assumption depending only on the stress triaxiality is presumably insufficient to judiciously describe the ductile fracture behaviour. Thus, Tvergaard and Needleman extended this model to account for nucleation and coalescence mechanisms and included also some parameters to improve the correlation with results obtained from unit cell computations [12]. Although, Gurson-like models can accurately describe the damage evolution for several applications they also revealed some drawbacks, namely: (i) no void shearing effect is included [14]; and (ii) due to the large number of parameters, its calibration can be a costly and laborious task. Therefore, to overcome these deficiencies, several extensions have been proposed, particularly to enable the successful prediction of failure under shear dominated stress states, by taking into account the sensitivity of the void volume fraction related to the Lode parameter ([15,4,16]).

An alternative type of coupled models was developed based on the phenomenological continuum theory, commonly referred as continuum damage mechanics (CDM). In this framework, the dissipation potential was built based on thermodynamic principles and the equivalent stress is coupled with a damage variable to describe the degradation of the material. The most widely known CDM model is the Lemaitre [17]. Several extensions of the original Lemaitre's model have also been proposed. However, these type of models often suffer from inaccurate predictions of strain localisation for pure shear stresses, (i.e., limited range of stress triaxiality) and particularly, under complex strain paths [18]. Some modifications have been introduced to overcome these limitations (see e.g., [19]). Nonetheless, it should be mentioned that when using coupled models, the constitutive models that describe the plastic and fracture behaviour need to be calibrated simultaneously. In this context, several calibration strategies have been proposed based on destructive and non-destructive tests. However, it is difficult to determine a unique set of parameters, due to the interaction between the material plastic and fracture behaviours. Moreover, the evaluation of the micromechanical based variables is an onerous task, since the analysis of voids evolution requires the use of techniques such as, tomography, metallographic observations, acoustic emission or induction spectroscopy [20].

The second category of ductile fracture models encompasses the uncoupled models. These models have been increasingly developed, since they present some advantages when compared with coupled models. Indeed, for uncoupled models, the damage accumulation is independent of the plastic dissipation potential. Moreover, their simple analytical forms, makes its calibration and implementation in numerical codes quite easy tasks ([21,22,10]). Besides, some works reported their good performance in failure prediction under complex loading paths ([18,23,24]).

The uncoupled ductile fracture models have been developed based on experimental investigations at both macroscopic and microscopic scales. On one hand, from the macroscopic point of view, fracture results from the progressive degradation of material, since it gradually loses its stiffness and consequently, its strength. On the other hand, from the microscopic point of view, the material fracture is the consequence of: (i) nucleation, growth and coalescence of micro voids, under large stress triaxiality; (ii) the presence of shear bands, related to low stress triaxiality; and (iii) combined shear and void growth mechanism, attributed to medium range of stress triaxiality.

Cockcroft and Latham, (C-L) model is among the first proposed uncoupled ductile fracture models [25]. This ductile fracture criterion considers that the main factor leading to material failure is the maximum principal tensile stress. It has been widely used for the prediction of fracture for bulk forming processes, such as forging [26] and in high-velocity perforation and penetration problems [27]. Nevertheless, its predictive fracture performance was shown only for the region of low and negative stress triaxiality ([28,29,30]); thus, it is restricted to this range [26]. This limitation is certainly related to its low flexibility (it involves only one damage parameter) ([26,28,31]).

Wierzbicki and co-workers assumed that when damage occurs in metallic materials, the accumulated equivalent plastic strain, expressed as a function of the stress state, reaches a critical value known as fracture strain [32]. It is known that the stress triaxiality influences the microscopic damage mechanisms, as previously mentioned. Thus, Mae and Wierzbicki proposed an uncoupled model (M-W) which only considers the dependence of fracture strain on the stress triaxiality and they evaluated its predictive ability using a combined experimental-numerical approach ([33,34]). Later, Wierzbicki and co-workers have shown that the fracture strain is limited within two bounding lines, corresponding to generalized shear or plane strain (lower bound) and to axisymmetric stress state (the normalized uniaxial tension or compression) (upper bound), respectively ([2,26]). They proposed the X-W model which defines the limits of the symmetric 3D fracture locus by a set of exponential functions. The two limits are defined by the effect of the normalized third invariant of the deviatoric stress tensor on fracture strain. However, the symmetric form of the fracture locus can limit the description of the material's ductility [35]. Therefore, a 3D uncoupled fracture locus was proposed by Bai and Wierzbicki (B-W model), based on three bounding limits [32]. The lower bound is the same (generalized shear or plane strain), but the symmetry between the stress states corresponding to axial symmetry in deviatoric tension and compression is no longer imposed, leading to two distinct upper bounds. The B-W model takes into account the effect of hydrostatic and deviatoric stresses on the ductile fracture, based on the stress triaxiality and Lode angle parameter. Such kind of models were successfully used to predict ductile fracture ([32,36,37]), for various applications in automotive, aerospace and marine industries ([35,38,21]). Nevertheless, the main challenge for these models was their ability to predict failure under non-proportional and complex loading conditions, for different classes of metallic materials.

Another research trend was followed for developing uncoupled ductile fracture models that is based on modified versions of fracture models. One of the most deep-rooted fracture model is the Mohr-Coulomb (M-C) [39], which has been extensively applied to predict fracture of non-metallic materials, such as soil and rocks (brittle materials, when compared to metals and their alloys). Since the mechanisms involved in the fracture behaviour of brittle materials are very different from those of ductile materials, the application of the M-C model was extended to metallic materials by introducing the influence of both the hydrostatic pressure and the Lode angle parameter on the fracture behaviour [40]. Bai and Wierzbicki successfully modified the M-C stress-based fracture criterion into a 3D fracture locus (MMC model) [40]. The performance assessment of the MMC model was achieved by its application for a diversity of

metallic materials, as reported in ([41,42,43,31,44,40,9,26,45,46]).

Despite the great success of the MMC model, it has been shown that it is consistently more suitable for failure prediction in shear-dominated stress states, rather than in ones controlled by void-growth and coalescence mechanisms [40]. Therefore, further modifications were brought to this model to improve its prediction accuracy for a wider range of stress states ([47,48]). Essentially, Tresca equivalent stress was substituted by the Hosford one, leading to the so-called Hosford-Coulomb (H-C) model [47]. The H-C model predicts fracture when the linear combination of the normal stress and the Hosford equivalent stress reaches a critical value. According to Ha et al. [49], the H-C model exhibits an improved performance for the low positive range of stress triaxiality in comparison with MMC model. It was applied to predict the ductile fracture initiation for several metallic materials, as reported in ([50,51,24,47,48,52,23]).

Additional uncoupled models were developed based on microscopic damage accumulation mechanisms, such as the nucleation, growth and shear of voids. Lou and Huh (L-H) model is as an example [29], which is characterized by the incorporation of a cut-off value, for which no fracture occurs, when the stress triaxiality is less than  $(-1/3)$ . This value is consistent with the observations reported in [53]. The L-H model was implemented in Abaqus/Explicit solver to predict the fracture behaviour of DP780 steel [29]. The results showed that for non-proportional loading conditions, the cut-off value could occur for different stress triaxiality values. Thus, this model was further modified by introducing a variable which takes into account the material microstructure effect on the stress triaxiality cut-off value [54]. In addition, the influence of the anisotropic behaviour of the material on ductile fracture was also included in the model [55]. L-H model was successfully applied to predict fracture for isotropic ([29,10]) and anisotropic materials ([56,55,57]). The results showed good fracture predictions under different loading conditions, such as tension and pure shear stress states [56].

Recently, Quach et al. proposed an uncoupled model to describe the anisotropic fracture behaviour of metallic sheets ([9,58]). The results showed that the Q-K model enables the prediction of fracture in a square cup drawing test performed with an 6014-T4 aluminium alloy [9].

The above-mentioned uncoupled models were used to solve engineering problems involving ductile fracture prediction, including the description of localization phenomena observed under complex loading conditions or/and for non-proportional loading paths. Consequently, it is evident that significant research efforts have been deployed to reveal the inherent mechanisms responsible for the ductile fracture behaviour of metals and their modelling. Despite the large number of available ductile fracture models, the selection of the appropriate one to accurately describe the fracture behaviour of metals is still a challenging task. The models' calibration results depend on the material, the number and the type of tests, which are related to the stress state range. Therefore, it is of paramount importance to study its effects, using several combinations of experimental tests, on the models' ability to reproduce experimental observations.

In this work, a calibration procedure is used to assess the effect of the set of experimental data selected on the parameter identification and on the fracture prediction ability of seven uncoupled ductile fracture models, as such thorough analysis has not been reported elsewhere. In this context, the same calibration procedure is applied to several sets of experimental tests, defining different identification strategies for the 2024-T351 aluminium alloy. One of the calibration strategies is then applied to the DP600 steel to evaluate to what extent the drawn conclusions are valid for other materials.

This manuscript is organized as follows. The next section presents the variables used to describe the stress state in uncoupled fracture models. A brief description of the seven uncoupled fracture models is presented in section 3. The available sets of experimental results for both materials are depicted in section 4, as well as the procedure used to identify the models' ductile fracture parameters. A detailed discussion of the results is presented in section 5 and the main conclusions are drawn in the last section.

## 2. Description of the stress state

Ductile fracture mechanisms are related to the loading conditions that the material is undergoing, i.e., to the stress state, which can be defined by the Cauchy stress tensor,  $\sigma$ . Regarding the ductile fracture mechanics, the stress state is usually described by two dimensionless parameters: the stress triaxiality  $\eta$  and the normalized Lode angle  $\bar{\theta}$ . These parameters can be defined based on the second and third invariants of the deviatoric stress tensor,  $s$ , expressed as follows:

$$J_2 = \frac{1}{2} s : s, \quad J_3 = \det(s) \quad (1)$$

$$s = \sigma - \sigma_m \mathbf{I} = \frac{1}{3} (\sigma_1 + \sigma_2 + \sigma_3) \quad (2)$$

where  $\sigma_1$ ,  $\sigma_2$  and  $\sigma_3$  are the principal stresses of  $\sigma$ , such that  $\sigma_1 \geq \sigma_2 \geq \sigma_3$ . The von Mises equivalent stress can be expressed as follows:

$$\bar{\sigma} = \sqrt{\frac{3}{2} s : s} = \sqrt{3J_2} = \sqrt{\frac{1}{2} [(\sigma_1 - \sigma_2)^2 + (\sigma_2 - \sigma_3)^2 + (\sigma_3 - \sigma_1)^2]} \quad (3)$$

The stress triaxiality is defined as the ratio between the hydrostatic stress and the von Mises equivalent stress:

$$\eta = \frac{\sigma_m}{\bar{\sigma}} \quad (4)$$

The stress triaxiality is considered as a fundamental factor of ductile fracture for metallic materials. In fact, the hydrostatic stress is the driving force of the nucleation and growth of voids. On one hand, high hydrostatic stress intensity leads to an increase in the voids' sizes. On the other hand, the deviatoric stresses are responsible for the change of the voids' geometry. In this context, it is also important to define the normalized third invariant of the deviatoric stress tensor, as follows:

$$\xi = \frac{27J_3}{2\sigma^3} = \frac{3\sqrt{3}J_3}{2J_2^{3/2}} \quad (5)$$

which characterizes the position of the second principal stress  $\sigma_2$ , with respect to the maximum  $\sigma_1$  and minimum  $\sigma_3$  principal stresses, such that it is bounded between  $-1$  and  $1$ . This normalized parameter  $\xi$  is related to the Lode angle  $\theta$  through the following relation:

$$\xi = \cos(3\theta) \quad (6)$$

such that the range for the Lode angle  $\theta$  is  $0 \leq \theta \leq \frac{\pi}{3}$ . Besides, it is also common to adopt the normalized Lode angle  $\bar{\theta}$ , defined by:

$$\bar{\theta} = 1 - \frac{6\theta}{\pi} = 1 - \frac{2}{\pi} \arccos(\xi), \text{ where } -1 \leq \bar{\theta} \leq 1 \quad (7)$$

which is also called Lode angle parameter.  $\bar{\theta} = 0$  corresponds to generalized shear or plane strain, while  $\bar{\theta} = -1$  and  $+1$  correspond to axisymmetric compression and tension, respectively. Finally, it should be noted that the standard expression of the Lode parameter, denoted by  $L$ , is defined as follows:

$$L = \frac{2\sigma_2 - \sigma_1 - \sigma_3}{\sigma_1 - \sigma_3} = \frac{3\tan\theta - \sqrt{3}}{\tan\theta + \sqrt{3}}, \text{ such that } -1 \leq L \leq 1 \quad (8)$$

In the particular case of plane stress condition (PSC), the hydrostatic pressure changes along the loading history, but the normalized Lode angle remains constant. Thus, the stress triaxiality and the normalized Lode angle parameter are related by the following expression [36]:

$$\bar{\theta} = 1 - \frac{2}{\pi} \arccos\left(-\frac{27}{2}\eta\left(\eta^2 - \frac{1}{3}\right)\right), \text{ for } -\frac{2}{3} \leq \eta \leq \frac{2}{3} \quad (9)$$

Alternatively, the normalized third invariant of the deviatoric stress tensor is expressed by:

$$\xi = \cos\left(\frac{\pi}{2}(1 - \bar{\theta})\right) = -\frac{27}{2}\eta\left(\eta^2 - \frac{1}{3}\right) \quad (10)$$

The assumption of plane stress state is widely adopted in the calibration strategies of uncoupled fracture models, because it simplifies the procedure due to the representation of the fracture locus in a 2D space (see Eq. (9)). Indeed, different types of engineering applications have been reported in literature, such as stamping of an anticlastic structure [60]), cross-die forming and cup drawing applications ([61,62]), incremental sheet metal forming [63], three-point bending on a hat assembly [52], laser-welded stiffened panel penetration tests [64], impact tests on flat and perforated plate [50], burring sheet metal [65], for which the PSC was assumed in the calibration procedure. Therefore, as far as we know, this assumption does not necessarily influence the accuracy of the predicted results. Moreover, the PSC is commonly accepted for thin walled metallic parts, including sheet metal forming processes.

### 3. Overview of the selected ductile fracture models

The seven uncoupled ductile fracture models selected represent a set of the ones that were proposed in, approximately, the last two decades. They all share a relatively low number of fracture parameters since they are phenomenological. In that sense, one could infer that the ones proposed in the first decade (i.e., the family of models developed by Wierzbicki et al. (X-W, 2005; B-W, 2007 and M-W, 2008)) are more flexible, due to the slightly higher number of damage parameters than the one adopted in the more recent models (i.e., Q-K, 2020; H-C 2014; L-H, 2013, MMC, 2010). Nevertheless, different approaches were adopted, in particular, to integrate the material plastic behaviour in the description of the fracture surface. In this context, it is important to compare the predictive ability of more recent with older models, which were more widely investigated (e.g., X-W, 2007; B-W, 2007 and M-W, 2008). In this section, the selected models are briefly described.

#### 3.1. Xue and Wierzbicki, 2005 (X-W) model

Bao and Wierzbicki [1] performed a series of experiments on a 2024-T351 aluminium alloy and confirmed that ductile fracture is a non-monotonic function of the stress triaxiality, as early suggested in [3] and [66]. However, the stress triaxiality is not sufficient to capture the influence of the multiaxial stress state on the material ductile failure behaviour. The important effect of the Lode angle parameter on damage prediction was shown in several studies (e.g., [67,43,26,40,5]). Both stress triaxiality and normalized third invariant of the deviatoric stress tensor were taken into account in the X-W model, which defines the fracture strain,  $\bar{\epsilon}_f$ , as follows:

$$\bar{\epsilon}_f(\eta, \xi) = C_1 e^{-C_2 \eta} - (C_1 e^{-C_2 \eta} - C_3 e^{-C_4 \eta})(1 - \xi^m)^n \quad (11)$$

where  $C_1 e^{-C_2 \eta}$  and  $C_3 e^{-C_4 \eta}$  are exponential functions that should be determined based on the equivalent strain to fracture under uniaxial compression,  $\bar{\epsilon}_f^{(-)}$ , uniaxial tension,  $\bar{\epsilon}_f^{(+)}$ , and plane strain,  $\bar{\epsilon}_f^{(0)}$ , such that:

$$\begin{cases} \bar{\epsilon}_f^{(0)} = \bar{\epsilon}_f(\eta, \xi \text{ or } \bar{\theta} = 0) = C_3 e^{-C_4 \eta} \\ \bar{\epsilon}_f^{(+)} = \bar{\epsilon}_f^{(-)} = \bar{\epsilon}_f(\eta, \xi \text{ or } \bar{\theta} = \pm 1) = C_1 e^{-C_2 \eta} \end{cases}$$

The exponent  $m$  must be an even integer in order to enable the description of the drop of material ductility due to  $\xi$  by an elliptic function, with a symmetry plane in  $\xi = 0$ . Some authors suggested to select the even integer closest to  $1/n$ , where  $n$  is the strain hardening exponent [2]. Therefore, the model has four damage parameters:  $C_1$ ,  $C_2$ ,  $C_3$  and  $C_4$ .

### 3.2. Bai and Wierzbicki, 2007 (B-W) model

B-W model corresponds to an asymmetric ductile fracture model that neglects the effect of the strain hardening exponent on the fracture strain, unlike the previous model ([32,35]). The dependence of the fracture strain on  $\eta$  is described by an exponential function, whereas for  $\xi$  it is assumed as parabolic. This model was developed based on three bounding limits, i.e., three values of  $\xi$ , corresponding to axial symmetry in deviatoric tension,  $\xi = +1$ , plane strain or generalized shear,  $\xi = 0$ , and axial symmetry in deviatoric compression,  $\xi = -1$ , respectively. The fracture strain locus is defined by

$$\bar{\epsilon}_f(\eta, \bar{\theta}) = \left[ \frac{1}{2} (D_1 e^{-D_2 \eta} + D_5 e^{-D_6 \eta}) - D_3 e^{-D_4 \eta} \right] \bar{\theta}^2 + \frac{1}{2} (D_1 e^{-D_2 \eta} - D_5 e^{-D_6 \eta}) \bar{\theta} + D_3 e^{-D_4 \eta} \quad (12)$$

In this case, the exponential functions should be determined based on the equivalent strain to fracture under uniaxial compression,  $\bar{\epsilon}_f^{(-)}$ , tension,  $\bar{\epsilon}_f^{(+)}$ , and plane strain,  $\bar{\epsilon}_f^{(0)}$ , such that:

$$\begin{cases} \bar{\epsilon}_f^{(-)} = \bar{\epsilon}_f(\eta, \xi \text{ or } \bar{\theta} = -1) = D_5 e^{-D_6 \eta} \\ \bar{\epsilon}_f^{(0)} = \bar{\epsilon}_f(\eta, \xi \text{ or } \bar{\theta} = 0) = D_3 e^{-D_4 \eta} \\ \bar{\epsilon}_f^{(+)} = \bar{\epsilon}_f(\eta, \xi \text{ or } \bar{\theta} = 1) = D_1 e^{-D_2 \eta} \end{cases}$$

This model has six parameters:  $D_1$ ,  $D_2$ ,  $D_3$ ,  $D_4$ ,  $D_5$  and  $D_6$ . The authors recommend the use of six types of specimen to carry out the experimental tests: tensile tests on smooth and notched round bars ( $\bar{\theta} = 1$ ), plane strain test ( $\bar{\theta} = 0$ ), flat grooved tension ( $\bar{\theta} = 0$ ), upsetting test and cylinder upsetting test ( $\bar{\theta} = -1$ ) [35].

### 3.3. Mae and Wierzbicki, 2008 (M-W) model

This simple empirical ductile fracture model considers only the influence of the stress triaxiality, which is known to control the fracture mechanism of coalescence, growth and nucleation of voids, or/and shear mode ([33,34]). This model is expressed in three branches, as follows:

$$\begin{cases} \bar{\epsilon}_f = \frac{D_1}{1 + 3\eta}, & -\frac{1}{3} \leq \eta \leq 0 \\ \bar{\epsilon}_f = \bar{\epsilon}_{f,t} + (\bar{\epsilon}_{f,t} - \bar{\epsilon}_{f,s})(3\eta - 1), & 0 \leq \eta \leq \frac{1}{3} \\ \bar{\epsilon}_f = D_2 e^{D_3 \eta} + D_4, & \frac{1}{3} \leq \eta \end{cases} \quad (13)$$

where  $\bar{\epsilon}_{f,t}$  and  $\bar{\epsilon}_{f,s}$  are the effective fracture strain under uniaxial tension and shear, respectively. The four model's damage parameters are  $D_1$ ,  $D_2$ ,  $D_3$  and  $D_4$ . However, as can be seen from Eq. (13),  $D_1 = \bar{\epsilon}_{f,s}$  and  $\bar{\epsilon}_{f,t} = D_2 e^{D_3/3} + D_4$ , which means that the parameters are not independent ([68,69]). M-W model was successfully applied in the prediction of ductile fracture for materials that experienced proportional loadings, for which the stress triaxiality remains constant [34].

### 3.4. Modified Mohr-Coulomb, 2010 (MMC) model

Originally, the Mohr and Coulomb criterion [39] was developed for brittle materials, such as soil and rocks. It incorporates a linear relationship between the shear,  $\tau$  and the normal  $\sigma_n$ , stress components and corresponds to the following relation:

$$\max(\tau + c_1 \sigma_n)_f = c_2 \quad (14)$$

where,  $c_1$  and  $c_2$  correspond to the model's parameters, such that fracture occurs when the linear combination of the shear and normal stresses reaches the critical value  $c_2$ . The main drawbacks of this model are the following: it can be only used under small plastic strains and it is pressure or stress triaxiality independent. Therefore, a modified version was proposed by Bai and Wierzbicki [40]. They

introduced a hardening rule, which incorporates the dependence on the Lode angle parameter and stress triaxiality. The Mohr and Coulomb model is defined in a Cartesian coordinate system, based on the principal stresses  $(\sigma_1, \sigma_2, \sigma_3)$ . Hence, the first step consists on its transformation to the spherical coordinate system, defined by the equivalent stress, the stress triaxiality and the Lode angle  $(\bar{\sigma}, \eta, \theta)$ . Assuming that the material is isotropic, the von Mises yield criterion can be adopted to determine the equivalent stress, as follows:

$$\bar{\sigma}_f = c_2 \left[ \sqrt{\frac{1+c_1^2}{3}} \cos\left(\frac{\pi}{6} - \theta\right) + c_1 \left( \eta + \frac{1}{3} \sin\left(\frac{\pi}{6} - \theta\right) \right) \right]^{-1} \quad (15)$$

Further details on this transformation can be found in [40] and [70]. Considering that the material's hardening behaviour can be described by a simple isotropic power-law.

$$\bar{\sigma} = A(\bar{\epsilon}^p)^n \quad (16)$$

The equivalent strain at fracture can be expressed as:

$$\bar{\epsilon}_f = \left[ \frac{A}{c_2} \left[ \sqrt{\frac{1+c_1^2}{3}} \cos\left(\frac{\bar{\theta}\pi}{6}\right) + c_1 \left( \eta + \frac{1}{3} \sin\left(\frac{\bar{\theta}\pi}{6}\right) \right) \right] \right]^{-\frac{1}{n}} \quad (17)$$

where,  $A$  and  $n$  are the hardening parameters and  $\bar{\epsilon}^p$  is the equivalent plastic strain. However, this expression neglects the influence of the hydrostatic pressure and normalized Lode angle parameter on the hardening behaviour of materials. Therefore, Bai and co-workers proposed a generalized hardening rule with pressure and Lode angle dependence in the form:

$$\bar{\sigma} = A \bar{\epsilon}_f \left[ c_3 + \frac{\sqrt{3}}{2 - \sqrt{3}} (1 - c_3) \left( \sec\left(\frac{\bar{\theta}\pi}{6}\right) - 1 \right) \right] \quad (18)$$

where  $c_3$  constant defines the shape of the yield locus. For example, if the value of  $c_3$  is equal to 1, the yield surface corresponds to von Mises yield criterion, while for  $c_3 = \sqrt{3}/2$  it corresponds to Tresca yield criterion [40]. Thus, the modified Mohr-Coulomb model becomes:

$$\bar{\epsilon}_f = \left[ \frac{A}{c_2} \left[ c_3 + \frac{\sqrt{3}}{2 - \sqrt{3}} (1 - c_3) \left( \sec\left(\frac{\bar{\theta}\pi}{6}\right) - 1 \right) \right] \cdot \left[ \sqrt{\frac{1+c_1^2}{3}} \cos\left(\frac{\bar{\theta}\pi}{6}\right) + c_1 \left( \eta + \frac{1}{3} \sin\left(\frac{\bar{\theta}\pi}{6}\right) \right) \right] \right]^{-\frac{1}{n}} \quad (19)$$

where  $c_1$ ,  $c_2$  and  $c_3$  are the three parameters of the modified Mohr-Coulomb model. This model was extended to enable an improved distinction between tension and compression stress states. In that case, the model considers four parameters:  $c_\theta^{ax}$ ,  $c_\theta^s$ ,  $c_1$  and  $c_2$ , such that the equivalent strain to fracture is defined by:

$$\bar{\epsilon}_f = \left[ \frac{A}{c_2} \left[ c_\theta^s + \frac{\sqrt{3}}{2 - \sqrt{3}} (c_\theta^{ax} - c_\theta^s) \left( \sec\left(\frac{\bar{\theta}\pi}{6}\right) - 1 \right) \right] \cdot \left[ \sqrt{\frac{1+c_1^2}{3}} \cos\left(\frac{\bar{\theta}\pi}{6}\right) + c_1 \left( \eta + \frac{1}{3} \sin\left(\frac{\bar{\theta}\pi}{6}\right) \right) \right] \right]^{-\frac{1}{n}} \quad (20)$$

where the parameter  $c_\theta^{ax}$  is defined as follows:

$$c_\theta^{ax} = \begin{cases} 1 & \text{for } \bar{\theta} \geq 0 \\ c_\theta^c & \text{for } \bar{\theta} < 0 \end{cases}$$

The parameter  $c_\theta^s$  controls the asymmetry of the yield surface and consequently the fracture locus [71]; while  $c_\theta^c$  controls its dependence on  $\bar{\theta}$  [40]. To identify the parameters  $c_\theta^s$  and  $c_\theta^c$ , the authors recommended the use of tests under the following conditions: axial-symmetric compression, plane strain and axial-symmetric tension. They mentioned that these parameters can also be determined from plasticity tests, since they are involved in the determination of the yield surface shape [40]. Nevertheless, the MMC model adopted in this work is the one given in Eq. (19), i.e., it has three parameters:  $c_1$ ,  $c_2$ ,  $c_3$ . Note that in this case, it is also necessary to identify the hardening parameters  $A$ ,  $n$ , which can be determined using the stress-strain curve obtained from an uniaxial tensile test [2].

### 3.5. Lou and Huh, 2013 (L-H) model

This fracture model describes the micro-mechanisms of nucleation of voids, growth and coalescence by the stress triaxiality, and the shear mode by the normalized maximum shear stress,  $\tau_{\max}$ , as follows ([29,31]):

$$\left( \frac{2\tau_{\max}}{\bar{\sigma}} \right)^{c_1} \left( \frac{\langle 1 + 3\eta \rangle}{2} \right)^{c_2} \bar{\epsilon}_f = c_3 \quad (21)$$

where  $c_1$ ,  $c_2$  and  $c_3$  are model parameters and.



$$\tau_{\max} = \frac{(\sigma_1 - \sigma_3)}{2} \quad (22)$$

Using the relationship between the principal stresses  $(\sigma_1, \sigma_2, \sigma_3)$ , the Lode parameter,  $L$  (Eq. (8)) and stress triaxiality,  $\eta$  (Eq. (4)), the L-H, 2013 model can also be written as follows:

$$\left( \frac{2}{\sqrt{L^2 + 3}} \right)^{c_1} \left( \frac{\langle f(\eta, L) \rangle}{f(\frac{1}{3}, -1)} \right)^{c_2} \bar{\epsilon}_f = c_3 \quad (23)$$

since

$$\frac{2\tau_{\max}}{\bar{\sigma}} = \frac{2}{\sqrt{L^2 + 3}} \quad (24)$$

and

$$f(\eta, L) = \frac{\sigma_1}{\bar{\sigma}} = \eta + \frac{3 - L}{3\sqrt{L^2 + 3}} \quad (25)$$

where  $\langle \rangle$  represents the Macaulay brackets. The authors initially suggested the introduction of a constant cut-off value for the stress triaxiality. However, they found that the cut-off value for the stress triaxiality can be affected by the temperature, the material microstructure ([72,31]) and the stress state, through the Lode parameter ([31,54]). Therefore, they proposed an extended version, defined as follows:

$$\left( \frac{2\tau_{\max}}{\bar{\sigma}} \right)^{c_1} \left( \frac{\langle f(\eta, L, C) \rangle}{f(\frac{1}{3}, -1, C)} \right)^{c_2} \bar{\epsilon}_f = c_3 \quad (26)$$

with

$$f(\eta, L, C) = \frac{\sigma_1}{\bar{\sigma}} + C = \eta + \frac{3 - L}{3\sqrt{L^2 + 3}} + C \quad (27)$$

The two terms,  $2\tau_{\max}/\bar{\sigma}$  and  $f(\eta, L, C)$  are used to describe the shear voids coalescence and the voids growth, respectively.  $f(\eta, L, C)$  represents the dependency on  $L$  of the cut-off value for the  $\eta$ . As previously mentioned, this cut-off value is also dependent on the material microstructure. Therefore, the  $C$  parameter was also introduced to define the height parameter of the cut-off value of triaxiality. This model encompasses a total of four parameters:  $c_1$ ,  $c_2$ ,  $c_3$  and  $C$ . The fracture parameter  $C$  determines the ductile fracture occurrence for a certain loading condition. For instance, for  $C = 0$ , the cut-off value of the  $\eta$  is associated to the condition  $\sigma_1 = 0$  (see, Eq. (27)); while for  $C > 0$ , it corresponds to low stress triaxiality value. L-H model was successfully used in the numerical analysis for metal forming processes, under monotonic loading conditions, including shear dominated stress states, alike the MMC model [73].

### 3.6. Hosford-Coulomb, 2014 (H-C) model

According to several experimental and theoretical studies, fracture model based on Mohr-Coulomb criterion combined with isotropic yield criterion enable accurate predictions of fracture under stress states ranging from shear to tension ([31,48,52]). Therefore, the M-C model was improved by substituting Tresca equivalent stress (see Eq. (13)) by Hosford's one [47], to enhance the agreement between the experimental data and the model predictions [48]. The form of the M-C model expressed in terms of principal stresses is defined as follows:

$$(\sigma_1 - \sigma_3) + c_1(\sigma_1 + \sigma_3) = 2c_2 \quad (28)$$

and the Hosford equivalent stress is given by

$$\bar{\sigma}_{HF} = \left\{ \frac{1}{2} ((\sigma_1 - \sigma_2)^a + (\sigma_2 - \sigma_3)^a + (\sigma_1 - \sigma_3)^a) \right\}^{\frac{1}{a}} \quad (29)$$

where  $a$  presents the Hosford exponent. Note that the Hosford criterion becomes non-convex for  $a < 1$ , but there is no restriction with respect to convexity when it is used as localization criterion; thus, it is recommended to consider  $(0 < a \leq 2)$  [48]. The H-C fracture model is defined in terms of the Hosford equivalent stress and normal stress as follows:

$$\bar{\sigma}_{HF} + c(\sigma_1 + \sigma_3) = b_0 \quad (30)$$

where  $c = \frac{c_1}{\sqrt{1+c_1^2}}$  and  $b_0 = \frac{2c_2}{\sqrt{1+c_1^2}}$ .



As for the MMC model, this ductile fracture model can also be expressed as a function of the stress triaxiality, the Lode angle parameter and the mean stress, by using the geometrical construction of the principal stresses, deviatoric stresses and the Lode angle on the deviatoric plane, as shown in Fig. 1.

The deviatoric principal stress can be expressed in terms of equivalent stress and Lode angle as follows:

$$\begin{cases} \sqrt{\frac{3}{2}}s_1 = \sqrt{\frac{2}{3}}\bar{\sigma}\cos(\theta) \\ \sqrt{\frac{3}{2}}s_2 = \sqrt{\frac{2}{3}}\bar{\sigma}\cos\left(\frac{2\pi}{3}-\theta\right) \\ \sqrt{\frac{3}{2}}s_3 = \sqrt{\frac{2}{3}}\bar{\sigma}\cos\left(\frac{4\pi}{3}-\theta\right) \end{cases} \quad (31)$$

Using the relationship between the principal stresses and the principal deviatoric stresses,  $\sigma_i = \sigma_m + s_i$ ,  $i = \{1..3\}$ , the principal stresses are defined as [40]:

$$\begin{cases} \sigma_1 = \left(1 + \frac{2\cos(\theta)}{3\eta}\right)\sigma_m = \left(1 + \frac{f_1}{\eta}\right)\sigma_m \\ \sigma_2 = \left(1 + \frac{2\cos\left(\frac{2\pi}{3}-\theta\right)}{3\eta}\right)\sigma_m = \left(1 + \frac{f_2}{\eta}\right)\sigma_m \\ \sigma_3 = \left(1 + \frac{2\cos\left(\frac{4\pi}{3}-\theta\right)}{3\eta}\right)\sigma_m = \left(1 + \frac{f_3}{\eta}\right)\sigma_m \end{cases} \quad (32)$$

where either the Lode angle or the normalized Lode angle parameter-dependent functions [24] are used. The latter are defined as follows:

$$\begin{cases} f_1(\bar{\theta}) = \frac{2}{3}\cos\left(\frac{\pi}{6}(1-\bar{\theta})\right) \\ f_2(\bar{\theta}) = \frac{2}{3}\cos\left(\frac{\pi}{6}(3+\bar{\theta})\right) \\ f_3(\bar{\theta}) = \frac{2}{3}\cos\left(\frac{\pi}{6}(1+\bar{\theta})\right) \end{cases} \text{ where } \bar{\theta} = 1 - \frac{6\theta}{\pi} \quad (33)$$

Then, by substituting the Eq. (32) into Eq. (30), the resulting Hosford-Coulomb fracture surface can be expressed in the  $(\eta, \bar{\theta}, \bar{\sigma})$  space as:

$$\bar{\sigma}(\eta, \bar{\theta}) = \frac{b_0}{\left\{ \frac{1}{2} \left( (f_1 - f_2)^a + (f_2 - f_3)^a + (f_1 - f_3)^a \right) \right\}^{\frac{1}{a}} + c(2\eta + f_1 + f_3)} \quad (34)$$

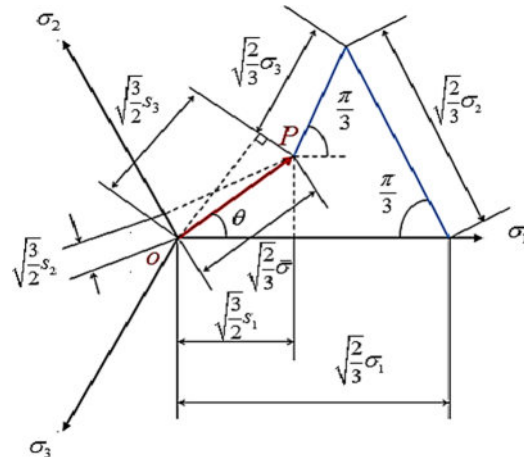


Fig. 1. Geometrical construction of the principal stresses, deviatoric stresses and the Lode angle on the deviatoric plane [26].

The transformation of the Hosford-Coulomb criterion from the stress space  $(\eta, \bar{\theta}, \bar{\sigma})$  into the strain space  $(\eta, \bar{\theta}, \bar{\epsilon}_f)$  requires the selection of an isotropic hardening law. If the simple isotropic power-law (see Eq. (16)) is considered, the H-C fracture model can be expressed as follows:

$$\bar{\epsilon}_f(\eta, \bar{\theta}) = \left( \frac{b_0}{A} \right)^{\frac{1}{n}} \left( \left\{ \frac{1}{2} ((f_1 - f_2)^a + (f_2 - f_3)^a + (f_1 - f_3)^a) \right\}^{\frac{1}{a}} + c(2\eta + f_1 + f_3) \right)^{-\frac{1}{n}} \quad (35)$$

Some authors proposed its generalization to allow the use of a more general isotropic hardening law, expressed as follows [47]:

$$\bar{\epsilon}_f(\eta, \bar{\theta}) = b(1 + c)^{\frac{1}{n}} \left( \left\{ \frac{1}{2} ((f_1 - f_2)^a + (f_2 - f_3)^a + (f_1 - f_3)^a) \right\}^{\frac{1}{a}} + c(2\eta + f_1 + f_3) \right)^{-\frac{1}{n}} \quad (36)$$

In this form, the H-C ductile fracture model has three parameters:  $a$ ,  $b$  and  $c$ , i.e. the hardening law parameters are identified in conjunction with the fracture ones, except for  $n$  which is assumed to be the equal to the one determined with the power isotropic law. This later form is the one adopted in this work. This model was calibrated using an extensive experimental database, including the analysis of localization and void fraction evolution. Besides, numerical simulations were performed to assess its predictive performances [74].

### 3.7. Quach et al., 2020 (Q-K) model

Quach et al. claimed that most ductile fracture models cannot describe ductile fracture for various stress state, because they do not take into account all the macroscopic and microscopic mechanisms involved [9]. For instance, the empirical model proposed by Bao and Wierzbicki [53] considers the effect of the maximum principal stress, expressed in terms of the stress triaxiality, but neglects the effect of maximum shear stress, expressed by the Lode angle parameter. On the other hand, the MMC model does not include any micro-mechanisms. Therefore, Quach et al., proposed a new ductile fracture model (Q-K), taking into account the effect of both macroscopic and microscopic mechanisms on ductile fracture prediction, based on extensive studies and experimental observations. The Q-K model is expressed as follows ([9,58]):

$$\bar{\epsilon}_f = \frac{C_1}{\left( \frac{\sigma_1}{\sigma} + \frac{\tau_{\max}}{\sigma} \right)^{C_2} \left[ (3 + \sqrt{3} C_3) \left( \frac{\tau_{\max}}{\sigma} \right) - C_3 \right]} \quad (37)$$

where  $C_1$ ,  $C_2$  and  $C_3$  are the material parameters. This expression highlights that, from the macroscopic point of view, the proposed model considers the effect of both the maximum principal stress as well as the maximum shear stress. This fracture model is presented in function of the principal stresses, but using Eq. (32), it can be formulated as follows:

$$\bar{\epsilon}_f(\eta, L) = \frac{C_1}{(g_1[\eta, L])^{C_2} (g_2[L])} \quad (38)$$

where

$$\begin{cases} g_1[\eta, L] = \eta + \frac{3 - L}{3\sqrt{L^2 + 3}} + \frac{1}{\sqrt{L^2 + 3}} \\ g_2[L] = \frac{3 + \sqrt{3} C_3}{\sqrt{L^2 + 3}} - C_3 \end{cases}$$

From the microscopic point of view, the influence of both maximum principal stress and normalized maximum shear stress on the void growth evolution are expressed in terms of both stress triaxiality and Lode parameter in the function  $g_1[\eta, L]$ . The effect of secondary voids and rotation of voids during void coalescence, which is governed by maximum shear stress, is considered as a function of Lode parameter, as established in the function  $g_2[L]$ .

## 4. Experimental database and calibration procedure

Two distinct materials were selected, namely 2024-T351 aluminium alloy and DP600 steel. For the 2024-T351, we revisit the experimental tests reported in [1,40,77,78] that were also broadly used to study the predictive ability of various ductile fracture models, in a wide range of engineering applications [35,8,9]. Therefore, this data could be well-established as a benchmark for calibration and verification of uncoupled ductile fracture models. For the DP600 dual phase steel, we revisit the experimental dataset obtained by Basaran [59], which was used to study the predictive ability of various ductile fracture models in the positive range of the stress triaxiality. In this study, the experimental data is applied also to compare the fracture predictive ability of seven uncoupled models for the same range of stress triaxiality. These materials were selected based on the diversity and abundance of experimental results.

#### 4.1. Experimental database: 2024-T351 aluminium alloy

In order to cover a wide range of stress states, different samples were used for the 2024-T351 aluminium alloy, as shown in Fig. 2 ([2,35,79,80,54]). According to these latter references, the stress state changes during the test, although the test conditions attempt to impose monotonic loading paths. This presents a substantial issue for the calibration of the fracture models. For this reason, for each test, the stress state was analysed using a combined experimental and numerical approach [79]. Table 1 summarizes, for the 2024-T351, the average value of stress triaxiality and normalized Lode angle determined using this approach along with the equivalent strain to fracture. The set of 29 tests was divided into two subsets. The first subset includes tests performed under PSC (from #1 to #17) that was used for the identification of models' ductile fracture parameters. The second subset comprises tests carried out in the positive stress triaxiality range (from #18 to 29), which was used to assess the fracture predictive ability of the calibrated models.

#### 4.2. Experimental database: DP600 steel

The set of experimental tests carried out for the DP600 [59] used different types of samples, as shown in Fig. 3. Table 2 summarizes the average value of stress triaxiality and normalized Lode angle along with the equivalent strain to fracture. The set of 18 experimental tests was divided into two subsets: the first comprises tests performed under PSC (from #1 to #6) and was used for the calibration of the ductile fracture models; the second subset includes tests carried out in the positive stress triaxiality range (from #7 to #18) and was used to verify the accuracy of the calibrated models to predict failure.

#### 4.3. Calibration procedure of ductile fracture models

The models were calibrated using a procedure to solve an optimization problem, in which the objective function corresponds to the gap between the experimental fracture strain and the value predicted by the ductile fracture model, expressed as follows:

$$Err = \underset{(\psi_1, \psi_2, \dots, \psi_n)}{\text{Min}} (Error) = \underset{(\psi_1, \psi_2, \dots, \psi_n)}{\text{Min}} \left[ \frac{1}{N} \sum_{i=1}^N \left| \frac{\bar{\epsilon}_{f_{\text{Predicted},i}} - \bar{\epsilon}_{f_{\text{Experimental},i}}}{\bar{\epsilon}_{f_{\text{Experimental},i}}} \right| \right] \quad (39)$$

where  $(\psi_1, \psi_2, \dots, \psi_n)$  denote the ductile fracture parameters,  $N$  is the total number of tests considered, and  $\bar{\epsilon}_{f_{\text{Experimental},i}}$  and  $\bar{\epsilon}_{f_{\text{Predicted},i}}$  correspond to the experimental and predicted fracture strain values, for the same test  $i$ , respectively.

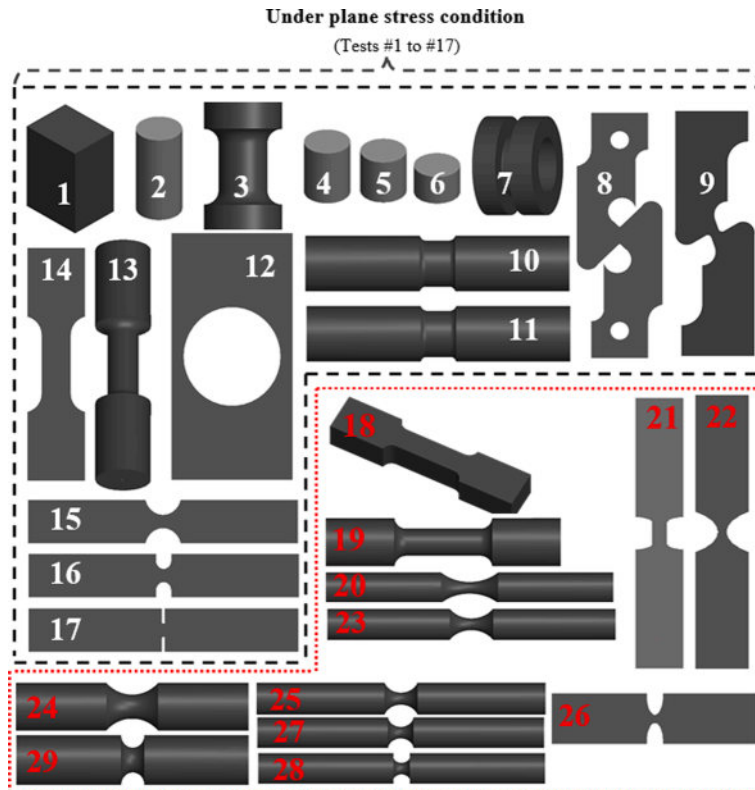


Fig. 2. Geometries of the specimens used in the experimental tests for 2024-T351 aluminium alloy (adapted from [1,79]).

**Table 1**

Experimental results of stress state and fracture strains for the 2024-T351 aluminium alloy ([1,40,77,78]).

Test #	Specimens	$\eta$	$\bar{\theta}$	$L$	$\xi$	$\bar{\epsilon}_f^p$
1	Bi-axial compression	-0.496	-0.398	0.367	-0.5852	0.349
2	Cylinder compression (d/h = 0.5)	-0.278	-0.8215	0.7946	-0.9609	0.4505
3	Round notched, Compression	-0.2476	-0.7141	0.6796	-0.9008	0.6217
4	Cylinder compression (d/h = 0.8)	-0.2339	-0.6809	0.6451	-0.8769	0.38
5	Cylinder compression (d/h = 1.0)	-0.2326	-0.6794	0.6435	-0.8758	0.3563
6	Cylinder compression (d/h = 1.5)	-0.2235	-0.6521	0.6155	-0.8543	0.341
7	Pure Torsion	0	0	0	0	0.288
8	Pure Shear	0.0124	0.0355	-0.0322	0.0557	0.2107
9	Combined Shear and Tension	0.1173	0.3381	-0.3099	0.5064	0.2613
10	Combined Tension and Torsion	0.1585	0.478	-0.4428	0.6822	0.2656
11	Torsion with constant axial tension	0.191	0.556	-0.519	0.7664	0.253
12	Plate with hole, Tension	0.3431	0.9661	-0.9594	0.9985	0.3099
13	Pipe, Tension	0.3557	0.9286	-0.9155	0.9937	0.3255
14	Dog-bone, Tension	0.357	0.9182	-0.9034	0.9917	0.4798
15	Thin notched specimen (r = 4.763 mm), Tension	0.4319	0.696	-0.6607	0.8881	0.2441
16	Thin notched specimen (r = 1.984 mm), Tension	0.4974	0.4486	-0.4145	0.6477	0.2204
17	Thin notched specimen (r = 0.396 mm), Tension	0.5648	0.0942	-0.0855	0.1474	0.1951
18	Solid square bar, Tension	0.3687	0.9992	-0.999	0.9999	0.3551
19	Round bar, Tension	0.4014	0.9992	-0.999	0.9999	0.4687
20	Notched bar(r = 14.503 mm), Tension	0.5243	1	-1	1	0.308
21	Flat-Grooved, Tension	0.603	0.0754	-0.0684	0.1181	0.21
22	Thick notched specimen(r = 13.970 mm), Tension	0.6052	0.1329	-0.1207	0.2072	0.1951
23	Notched bar(r = 9.144 mm), Tension	0.6072	1	-1	1	0.2909
24	Large notched bar (r = 12 mm), Tension	0.6264	0.9992	-0.999	0.9999	0.283
25	Notched bar(r = 6.096 mm), Tension	0.6765	1	-1	1	0.2727
26	Thick notched specimen(r = 4.763 mm), Tension	0.7304	0.0692	-0.0062	0.1084	0.2017
27	Notched bar(r = 4.470 mm), Tension	0.7631	1	-1	1	0.2447
28	Notched bar(r = 3.048 mm), Tension	0.8556	1	-1	1	0.2022
29	Small notched bar (r = 4 mm), Tension	0.9274	0.9984	-0.998	0.9999	0.1665

The objective function is minimized using the generalized reduced gradient (GRG) method for solving nonlinear problems, implemented in Excel. This method uses the gradient of the objective function as input to change the models' parameters until it attains a minimal value for the partial derivatives, i.e., an optimal solution is attained. The advantage of GRG nonlinear solver is its fastness; however, the main drawback is the dependence on the initial solution and the menace of falling into a local minimum, close to the initial input, instead of converging into the global optimal solution. To overcome this issue, the GRG multistart option was activated, in order to let the algorithm create a randomly distributed population of initial input values. By starting several times from different initial inputs, there is a much higher probability that the obtained solution falls into the global optimum.

The choice of the this calibration procedure is based on the fact that it enables achieving good results, when it was firstly used by Bao et al. [1] to calibrate fracture models for the 2024-T351 aluminium alloy and, subsequently, by Bai and Wierzbicki [35] as well as other researchers (see [8,81,82,23,9,45,83,46]). Thus, the performance of this calibration approach was satisfactorily demonstrated for distinct fracture models.

As previously stated in sections 4.1 and 4.2, the set of the experimental tests listed in Table 1 and 2, was split into two subsets. For 2024-T351 aluminium alloy, the first subset corresponds to 17 experimental tests (from #1 to #17), allowing to cover a range for  $\eta$  from -0.496 to 0.5648, and for  $\xi$  between -0.9609 and 0.9985. For DP600 steel, the first subset contains 6 tests (from #1 to #6) corresponding to the range from -0.06 to 0.66 for  $\eta$  and to the range from -1 to 0.96 for  $\xi$ . According to the PSC, the relationship between  $\eta$  and  $\bar{\theta}$  is established by Eq. (9) or between  $\eta$  and  $\xi$  by Eq. (10) [2]. The use of his relationship simplifies the analysis of the fracture models. Thus, the fracture locus can be represented in a 2D space:  $(\eta, \bar{\epsilon}_f)$ .

Depending on the model considered, the number of damage parameters varies from three to six, as listed in Table 3. However, some models also require the identification of the hardening law parameters (e.g., X-W, MMC and H-C models). In this work, a power hardening law was considered as expressed by Eq. (16)). The hardening parameters were identified using the stress-strain curve of the tensile test performed with the round bar and with the un-notched flat specimen, for 2024-T351 and DP600 steel, respectively ([2,59]). The obtained hardening parameters for 2024-T351 aluminium alloy and DP600 steel are  $A = 740$  MPa,  $n = 0.153$ , and  $A = 918.87$  MPa,  $n = 0.16$ , respectively. For the X-W model, the even integer closest to  $1/n$ , corresponding to  $m$ , is taken equal to 6, for both the 2024-T351 and the DP600.

It is noteworthy that the L-H model is 4 parameter-depend. The fourth parameter is denoted by  $C$  and it can also be identified using the optimization procedure [54]; however, it is recommended to choose the parameter  $C$  such that the  $\eta$  value for all fracture tests is higher than the cut-off value for  $\eta$  predicted by Eq. (27) [54]. In order to discuss the selection of this parameter, the influence of  $C$  on the cut-off value is analysed taking into account Eq. (27). Fig. 4 depicts the evolution of the cut-off value of  $\eta$  as a function of the Lode parameter considering different values of  $C$ , determined when Eq. (27) is equal to zero. Fig. 4 shows that the cut-off value of  $\eta$  decreases with the increase of  $C$ , such that when the value of  $C$  is higher than  $1/3$  (e.g.,  $C = 0.4$  or  $C = 0.5$ ), the cut-off value of  $\eta$  corresponding to Lode parameter  $L = 1$  will be lower than  $-2/3$ . However, all tests considered are under PSC, which implies that  $\eta$  is only varying

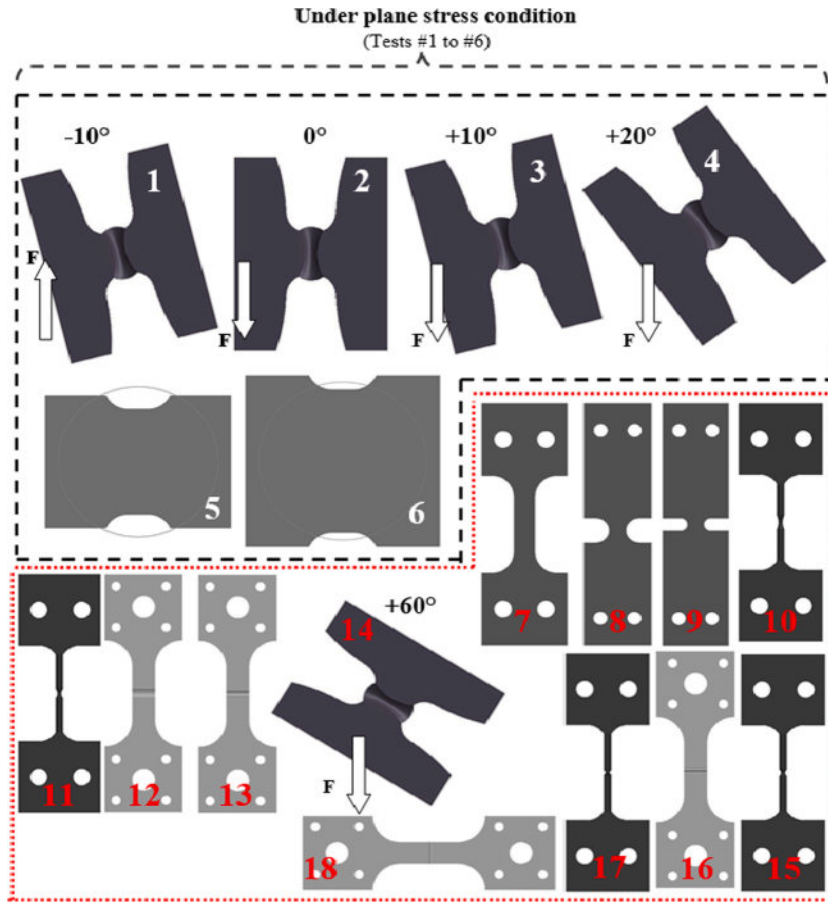


Fig. 3. Geometries of the specimens used in the experimental tests for the DP600 steel ([59]).

**Table 2**

Experimental results of stress state and fracture strains for the DP600 steel ([59]).

Test #	Specimens	$\eta$	$\bar{\theta}$	$L$	$\xi$	$\bar{\epsilon}_f^p$
1	Butterfly $-10^\circ$ , combined compression-shear	-0.06	-0.1608	0.146	-0.25	1.02
2	Butterfly $0^\circ$ , shear	0.07	0.1740	-0.158	0.27	1.08
3	Butterfly $10^\circ$ , combined shear-tension	0.18	0.4936	-0.458	0.7	0.7
4	Butterfly $20^\circ$ , combined shear-tension	0.34	0.8193	-0.792	0.96	0.95
5	Nakazima 1	0.64	-0.5303	0.494	-0.74	0.55
6	Nakazima 2	0.66	-1	1	-1	0.84
7	Smooth flat, tension	0.61	0.5209	-0.485	0.73	1.41
8	Notched flat 1 R = 4 mm, tension	0.63	0.4017	-0.37	0.59	0.81
9	Notched flat 2 R = 2 mm, tension	0.67	0.2344	-0.214	0.36	0.78
10	Notched round R = 4 mm, tension	0.7	1	-1	1	1.19
11	Notched round R = 2 mm, tension	0.74	1	-1	1	1.08
12	Grooved flat R = 4 mm, tension	0.76	0.0063	-0.006	0.01	0.98
13	Grooved flat R = 2 mm, tension	0.8	0.0063	-0.006	0.01	0.84
14	Butterfly $60^\circ$ , combined shear-tension	0.82	0.1806	-0.164	0.28	0.44
15	Notched round R = 1 mm, tension	0.82	1	-1	1	0.88
16	Grooved flat R = 1 mm, tension	0.88	0.0063	-0.006	0.01	0.7
17	Notched round R = 0.5 mm, tension	0.95	1	-1	1	0.67
18	Grooved flat R = 0.5 mm, tension	1.03	0.0063	-0.006	0.01	0.59

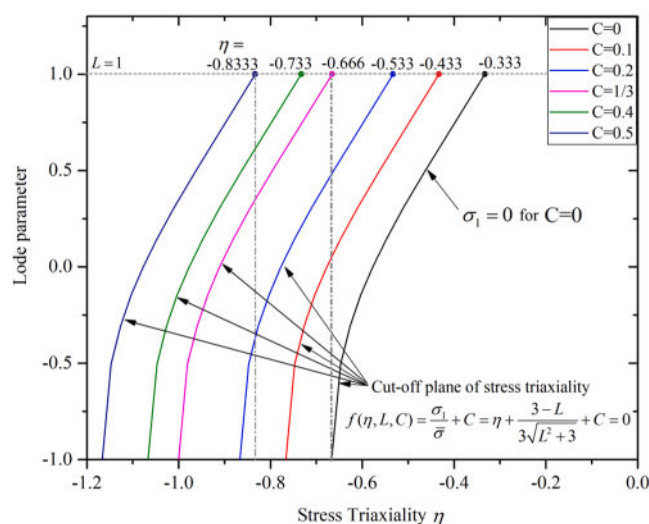
between  $-2/3$  and  $2/3$  and the Lode parameter  $L$  is in the interval  $[-1, 1]$ .

For the 2024-T351 aluminium alloy, according to test #1 (see, Table 1), the cut-off value of  $\eta$  should be lower than  $-0.496$ , for  $L = 0.367$ . This only justifies the adoption of the  $C$  parameter slightly higher than zero, to be certain that the fracture in compression conditions will occur for this value. Due to the lack of data, it was decided to consider  $C$  equal to  $1/3$  to assure that the cut-off value for the  $\eta$  will be lower or equal to  $-2/3$ . Unfortunately, for the DP600 steel, there is no experimental data for compression conditions.

**Table 3**

Damage parameters considered in the calibration procedure for each model.

Models	Number of damage parameters	Damage parameters
B-W	6	$D_1, D_2, D_3, D_4, D_5, D_6$
M-W	4	$D_1, D_2, D_3, D_4$
X-W	4	$C_1, C_2, C_3, C_4$
L-H	3	$c_1, c_2, c_3$
MMC	3	$c_1, c_2, c_3$
H-C	3	$a, b, c$
Q-K	3	$C_1, C_2, C_3$

**Fig. 4.** Cut-off plane of  $\eta$  for different values of  $C$  for the Lode parameter  $L$  between  $-1$  and  $1$ .

Thus, the same value was assumed for  $C$  parameter to ensure the targeted consistency for the calibration strategy adopted.

#### 4.4. Choice of stress states for models calibration and verification

The main purpose of this study is to assess the effect of using different type and number of tests on the identified models' parameters and then to evaluate the predictive ability of these models. In this sense, the available experimental data, for the 2024-T351 aluminium alloy, was split in different groups. Note that, the minimum number of experimental tests to be used for the calibration of the more flexible fracture model is 6 (see Table 3). Thus, groups of 6 tests were selected for which the stress states covered were carefully chosen in each group. Then, for comparison purpose with the calibration results obtained using the different groups of tests, the whole experimental dataset (Group 4) was used in the calibration of the models as routinely performed in previous works.

The different sets of 6 tests were carefully elicited from the 17 experimental tests available. The first calibration strategy uses the 6 following tests: #7, #8, #11, #14, #16, and #17, for which  $\eta$  ranges from 0 to 0.5648 and  $\xi$  is between 0 and 1. This is referred as Group 1. The second is referred as Group 2 and it is composed of the following 6 tests: #2, #6, #8, #10, #13 and #16, as listed in Table 1, for which  $\eta$  ranges from  $-0.278$  to  $0.4974$ , and  $\xi$  is between  $-0.9609$  and  $0.9937$ . These 6 tests were selected to analyse the influence of a wider amplitude for  $\xi$ . The third is referred as Group 3 and includes the following 6 experimental tests: #3, #4, #7, #11, #14 and #17, as shown in Table 1. In this group, the  $\eta$  ranges from  $-0.2476$  to  $0.5648$  and  $\xi$  ranges from  $-0.908$  to  $0.9917$ . Therefore, Group 2 covers a slightly lower range of  $\eta$  when compared to Group 3 and a similar range for  $\xi$ . More importantly, they present dissimilar equivalent strains to fracture, particularly between tests (#2, #3) and (#13, #14). Therefore, it allows to study the influence of considering different types of tests, for the same range of stress states. The last group, referred as Group 4, uses the full set of 17 experimental tests. This means that the whole range of available  $\eta$  and  $\xi$  values is covered. Thus, this group shows a slight increase of the  $\eta$  range, when compared with the ones used in the previous groups and a similar range for  $\xi$ .

For the DP600 steel, due to the lack of experimental data, only one group of 6 tests is considered in the calibration procedure. The group of 6 tests are labelled from #1 to #6 (see, Table 2). This means that they cover a range for  $\eta$  from  $-0.06$  to  $0.666$  and for  $\xi$  from  $-1$  to  $0.96$ . The comparison with the ranges considered in the groups used for 2024-T351 show that the more similar is Group 2, although it covers a slightly higher range of  $\eta$ . Group 1 presents a more similar range for  $\eta$ , but a lower range for  $\xi$ . Therefore, both groups are analysed in the comparative study concerning the predictive ability of the fracture models, for both materials.

The predictive ability of the calibrated fracture models was assessed based on the comparison between predicted fracture strain and



the observed one. For the 2024-T351 aluminium alloy, the subset of tests from #18 to #29 is considered. For the DP600 steel, the subset of tests from #7 to #18 is applied. For both materials, these subsets correspond to tests performed in the high  $\eta$  range, i.e.,  $\eta \geq 1/3$ . According to many authors (see e.g. [40,31]), the fracture occurrence in smooth and notched round bars or flat specimens, subjected to tension, is governed by the void growth and linkage of micro-cracks mechanisms. However, in compression, the shear mode dominates. Unfortunately, such fracture mechanisms are not properly captured by most of the ductile fracture models. In this context, it is important to assess the accuracy of the fracture prediction under the upper bound assumption, i.e.,  $\xi = +1$  and in the triaxial loading state, as occurs for the experimental set of tests from #18 to #29, for 2024-T351, and from #7 to #18 for DP600. Note that the test subjected to bi-axial compression loading (test #1) was considered neither in the calibration nor in the verification of the prediction ability of M-W model, because of the existence of a cut-off value of  $\eta$  equal to  $-1/3$ .

## 5. Results and discussion

This section starts with the analysis of the influence of the set of data selected on the calibration and predictive ability of the seven uncoupled models. This study is performed for the 2024-T35 aluminium alloy. Afterwards, the results obtained for both materials are analysed in order to assess to what extent the conclusions drawn for 2024-T351 can be extended to other materials. The average error values presented, either for the calibration or for the verification of the fracture models prediction ability is based on Eq. (39).

### 5.1. Analysis of the effect of the experimental dataset on the fracture models for 2024-T351

#### 5.1.1. Analysis of the calibration error

As previously mentioned, four groups of tests were used to calibrate the seven fracture models, Group  $I$ , where  $I = \{1, 2, 3, 4\}$ . The identified damage parameters are listed in Table 4. Groups 1, 2 and 3 consist of only 6 tests, while Group 4 considers 17 tests in the calibration procedure. Therefore, the average calibration error is calculated considering different types and number of tests. For all Groups, the calibration error is obtained at end of the optimization procedure, i.e. corresponds to the minimum of the objective function (Eq. (39)) for the specific set of tests considered. Nevertheless, for Groups 1, 2 and 3, the whole set of 17 tests is also used in the calculation of the average error. In other words, 11 tests among the 17 tests, which are not used in the calibration procedure, are considered. This allows to evaluate the impact of neglecting specific types of tests in the calibration procedure.

In Fig. 5, it is observed that the average calibration errors obtained for Group 1 and 2 are relatively lower than the ones obtained for Group 3. In addition, for all models, the average calibration errors for Groups 1, 2 and 4 are lower than 9%, except the M-W. Besides, for all models, the Group 2 has lower average calibration errors than Group 1, except for the M-W and the Q-K models.

It is somehow expected that the average error calculated considering tests not used in the calibration procedure is higher than the objective function value at the end of the optimization procedure. The magnitude of this error depends on the Group used for the models' calibration, as depicted in Fig. 5. It is interesting to note that, from the 6 tests sets, Group 2 leads to the lowest values for the

**Table 4**

Damage models parameters identified for 2024-T351 using Group 1, Group 2, Group 3 and Group 4 of experimental tests.

Model	Damage Parameters				
	Parameters	Group 1	Group 2	Group 3	Group 4
B-W	$D_1$	0.5451	0.5180	0.5242	0.4580
	$D_2$	0.001	1.1550	0.0001	1.0857
	$D_3$	0.21	0.2091	0.2875	0.2196
	$D_4$	0.0707	0.1342	0.7464	0.2984
	$D_5$	1.1476	0.4264	0.4426	0.342
	$D_6$	0.6333	1.0924	0.0001	1.7676
M-W	$D_1$	0.2069	0.1123	0.1597	0.1135
	$D_2$	0.6070	1.2256	0.3224	1.2259
	$D_3$	-2.937	-4.99	-2.171	-5.0
	$D_4$	0.079	0.1185	0.0	0.1185
X-W	$C_1$	2.8961	0.7227	0.9151	0.7062
	$C_2$	3.1124	1.2151	0.0001	1.1565
	$C_3$	0.2110	0.2677	0.2817	0.2732
	$C_4$	0.1392	0.4101	0.6505	0.4599
L-H $C = 1/3$	$c_1$	7.7668	3.947	7.3072	3.8076
	$c_2$	0.2984	0.3127	0.1810	0.3309
	$c_3$	0.5773	0.3591	0.5711	0.3540
MMC	$c_1$	0.0057	0.0288	0.0174	0.0377
	$c_2$ (MPa)	339.849	324.95	345.84	326.9
	$c_3$	1.0168	0.9477	1.0227	0.9467
H-C	$a$	0.9285	1.1621	1.4942	1.2351
	$b$	0.5897	0.3492	0.2596	0.334
	$c$	0.0137	0.0303	0.0461	0.0352
Q-K	$C_1$	0.3770	0.4711	0.401	0.4406
	$C_2$	0.2107	0.5836	0.3318	0.4348
	$C_3$	7.2130	4.1789	7.1962	3.5115



average error calculated with the 17 tests, which is also quite similar to the one calculated for Group 4. One could relate this to the wide range for the variables that define the stress states of the tests. However, group 2 and 3 presents a quite similar range for the stress state variables.

In order to better understand these results, Fig. 6 displays the relative error associated to each experimental test used in the calibration. Fig. 6 (a) shows for Group 1, that all models fail to describe the fracture strain for the pure torsion test (test #7), for which the relative errors are higher than 25%. Nevertheless, all models predict the fracture strains in the pure shear test (test #8) with an error lower than 10%. In this context, it is interesting to mention that these two experimental data points, corresponding to pure torsion (test #7) and pure shear (test #8) tests, present similar values for the stress state variables; however, the equivalent plastic strain values are slightly different (7.7% difference between the highest and the lowest).

In fact, the comparison with the relative errors obtained with Group 2, shown in Fig. 6 (b), indicates that it is the inclusion of test #7 that is contributing to the higher average calibration errors obtained with Group 1. These results seem to highlight the negative impact of the inclusion of tests with similar stress triaxiality and Lode parameter, but different fracture strains, which induce doubts about the fracture strain. However, it is noteworthy to remind that the measure of fracture strains is marred by uncertainty related to numerous sources. Fig. 6 (b) also shows that when using Group 2, there are no particular difficulties in capturing any particular test.

Fig. 6 (c) shows that, when using Group 3 for the models' calibration, all models, except M-W, present difficulties in capturing the compression of a round notched specimen (test #3), for which the relative errors are close to 40%. This indicates that it is the inclusion of this test that is contributing to the higher average calibration errors obtained with Group 3 (see Fig. 5). In this context, it is interesting to note that Group 4 also presents relative errors close to 40%, for all models. The fact that the average calibration error is lower, when compared with the one obtained with Group 3, is a consequence of the total number of tests considered (see Eq. (39)).

In order to further elucidate on the contribution of each test to the average error calculated with 17 tests, Fig. 7 presents the relative error values obtained for each test, performed under PSC, which has not been considered in the models' calibration for Group 1, 2 and 3. It is noteworthy that Group 1 globally presents high relative errors for tests with  $\xi < 0$ , which is probably related to the range considered for this parameter in the calibration set. Nevertheless, it also leads to worst predictions when comparing with Group 2, for tests with  $\xi = 1$ . In fact, Groups 1 and 3 lead to similar predictions for tests #12 and #13 (Plate with hole and pipe, under tension). It is also interesting to note that Groups 1 and 3 lead to similar average error values (calculated with all the tests in Fig. 5), for L-H, MMC, H-C, and Q-K models. However, the same average error is higher for models that are slightly more flexible, i.e., B-W, M-W and X-W models. For these models, the average errors obtained with the Group 1, when considering all tests under PSC are higher than 35%, as illustrated in Fig. 5. As previously mentioned, this high average error can be explained by the absence of experimental tests with  $\xi < 0$  in the calibration procedure (tests from #2 to #6, in Fig. 7 (a)). Therefore, B-W and X-W models seem to present a higher sensitivity to the stress state range considered in the calibration than the other models.

The sensitivity of the more flexible models to the dataset selected for calibration is particularly evident for the B-W, which attains an average calibration error close to zero only when Group 2 is selected. Nevertheless, as for Group 4, all models are not able to predict failure in the round notched compression test (test #3) and the tension test carried out on the dog-bone specimen (test #14). Fig. 5 highlights that the M-W model always leads to the highest values of the average calibration errors.

The analysis of Fig. 6 indicates that this model always presents more difficulties in capturing some of the calibration test values. For instance, when using Group 2, the relative errors values predicted by M-W model for the tests undergoing compression loading (test #2) and pure shear (test #8) are higher than 40% (Fig. 6 (b)), which obviously contribute to the increase of the average error value, when compared with other models. Note that for M-W model, the existence of cut-off value at the negative range of stress triaxiality

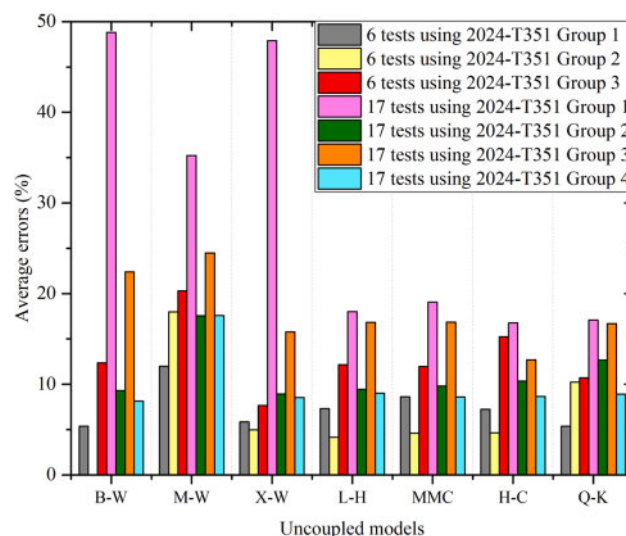
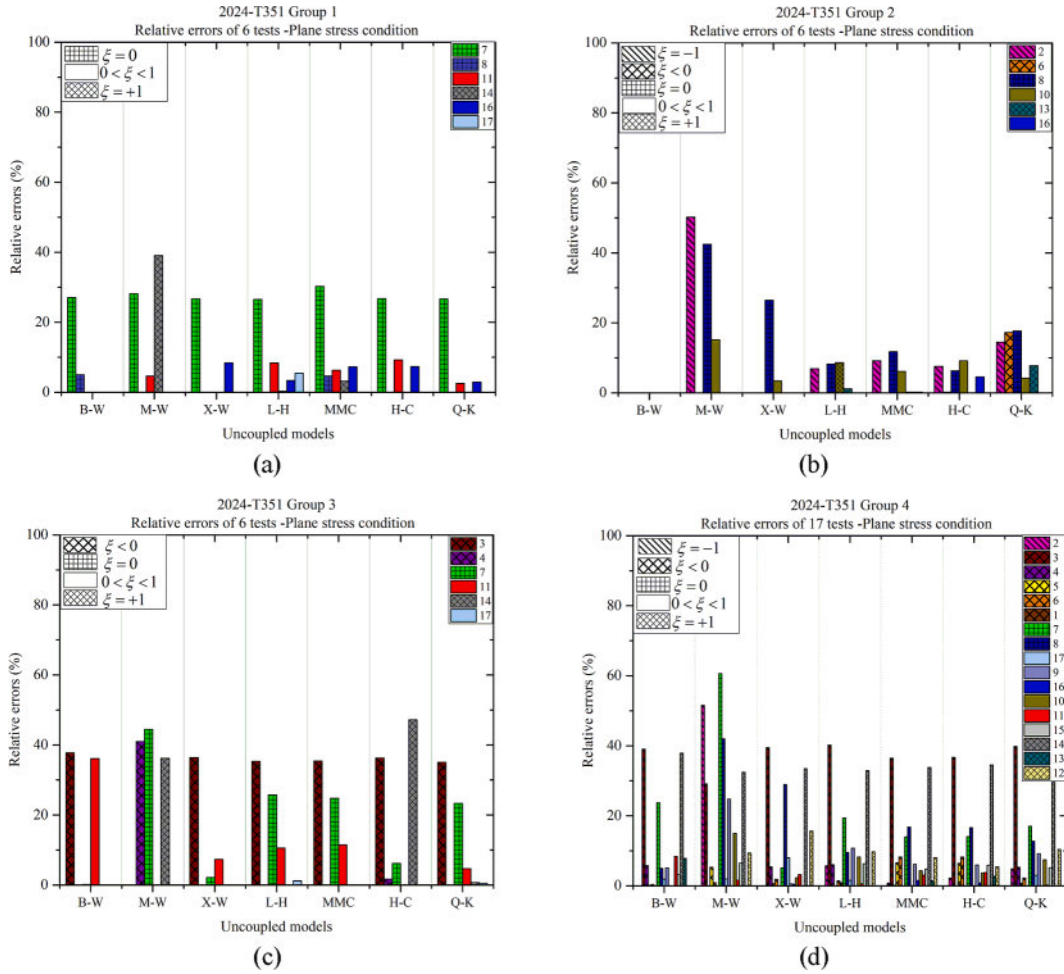


Fig. 5. Average errors obtained in the calibration procedure for 2024-T351: considering 6 tests in case of Group  $I$ ,  $I = \{1, 2, 3\}$  and 17 tests for all groups.



**Fig. 6.** Relative errors obtained in the calibration procedure performed for 2024-T351 using 6 tests: (a) Group 1; (b) Group 2; and (c) Group 3; and 17 tests (d) Group 4.

and its poor flexibility (only one damage parameter), limit its predictive capacity in this stress state range. Thus, when using Group 3, the M-W model fails to predict the fracture in the compression test on short cylinder specimen (test #4), pure torsion test (test #7), but also the tensile test carried out on the dog-bone specimen (test #14).

Fig. 8 shows the 2D fracture loci associated to the seven models that were calibrated using Group  $I$ , with  $I = \{1, 2, 3, 4\}$ . In this figure, the tests used in the calibration procedure, for each Group, are marked with white-coloured diamonds. Globally, for the same calibration group, the trend of the fracture strains obtained with the seven selected models are very similar. These are particularly evident for L-H, MMC and Q-K models. In fact, the group selected seems to have a bigger impact in the local peaks for  $\eta = -1/3$  and  $\eta = +1/3$  (see zone A and zone B in Fig. 8, respectively). Fig. 8 (a) and (b) show a significant difference in the fracture locus obtained using Group 1 and 2, for all models, especially in zone A and zone B. This is certainly related with the fact that Group 1 considers only the positive range of  $\eta$  and Lode angle parameter. Significant differences are also observed in the 2D fracture locus obtained by the selected models when considering the two groups with very similar ranges for the stress states but slightly different values of fracture strain, i.e. Group 2 and 3. The three tests (tests #3, #7, and #14 used by Group 3) present clearly higher values of equivalent strain to fracture, when compared with the neighbouring stress states (tests #2, #8, and #13 used by Group 2). Fig. 8 (c) shows that Group 3 leads to a shift of the 2D fracture locus upward, with a strong change in its shape, for all models, except B-W and H-C. The B-W, X-W and H-C models present a quite different trend for  $\eta = -1/3$  and  $\eta = +1/3$  (see zone A and B in Fig. 8 (c)). For the B-W model, the calibration using Group 3 shifts the fracture locus downward in the negative range of  $\eta$ . However, it presents a similar evolution of the equivalent strain to fracture as the other models, in the high range of  $\eta$ . Furthermore, the X-W model predicts higher values of the fracture strains for  $\eta = -1/3$  and  $\eta = +1/3$ , whatever the calibration group adopted. Moreover, it attains the highest magnitude for the fracture strain for  $\eta = +1/3$  when using Group 1 (zone B in Fig. 8 (a)). Thus, this model shows a higher sensitivity to the set of tests selected for the calibration than the other models. The fracture loci predicted by the H-C model using Group 3 is quite different of the ones obtained with the other models, since there is no strong increase of the fracture strain in the low range of  $\eta$  ( $0 \leq \eta \leq 1/3$ ), as shown in Fig. 8 (c). It is clear from Fig. 8 (b) and (d) that Group 2 and Group 4, lead to a similar trend of 2D fracture locus, except for B-W and Q-K models. The

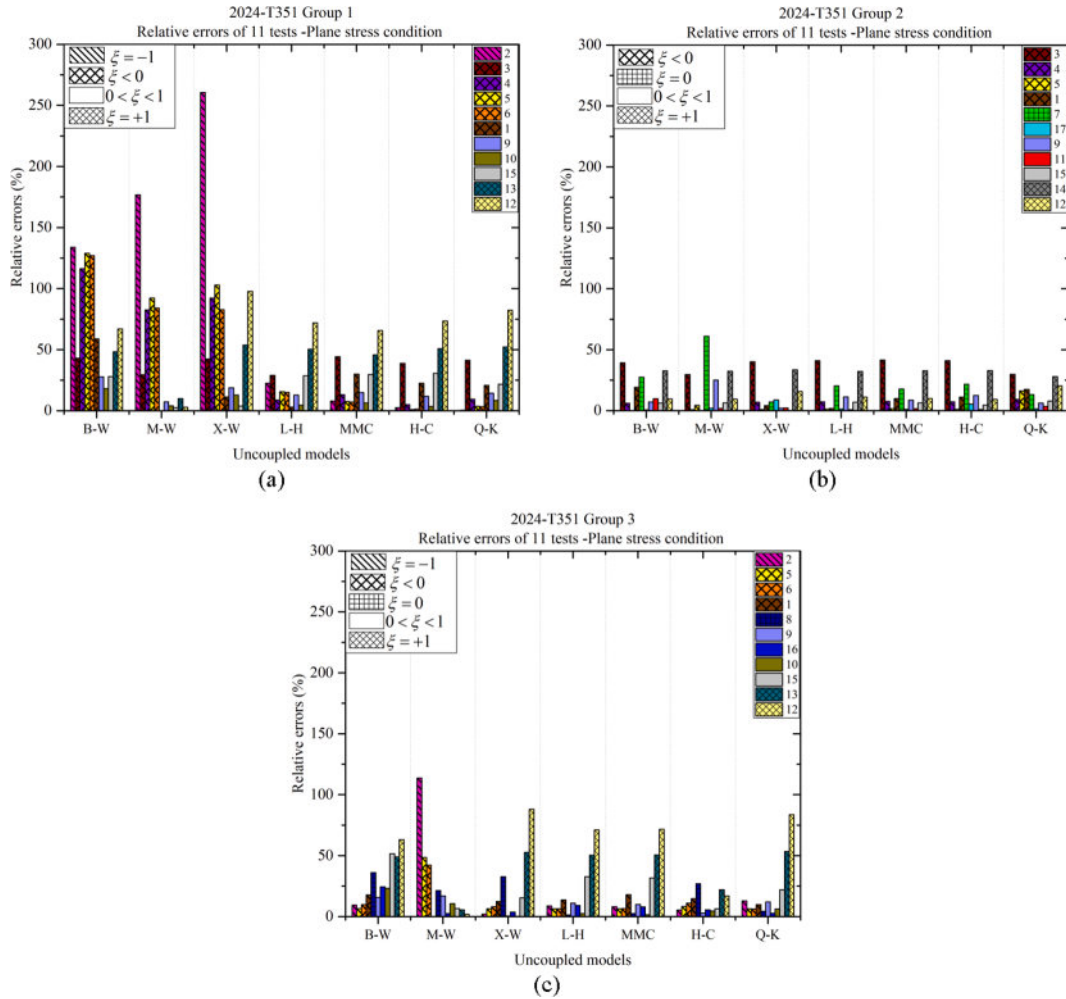


**Fig. 7.** Relative errors obtained in the calibration procedure performed for 2024-T351 using 6 tests, for the remaining 11 tests performed under PSC: (a) Group 1; (b) Group 2; and (c) Group 3.

fracture locus predicted by the B-W model with Group 2 is slightly concave for high  $\eta$  values while it becomes a little convex when using Group 4, particularly for  $\eta \geq 1/3$ . The Q-K model presents a quite different trend of the fracture locus, for the negative range of  $\eta$  (see zone A in Fig. 8), when comparing Group 2 with Group 4. The calibration using the 6 tests (Group 2 in Fig. 8 (b)) shifts the fracture locus upwards, for  $\eta = -1/3$ . The shift downwards of the 2D fracture locus observed for Group 4 seems to be related with the larger number of tests close to negative stress state values (tests #1 and #3–5).

In summary, the same calibration procedure performed with either different types and/or numbers of tests can lead to different average calibration errors, which tends to be lowest for the models that are more flexible. These models are also more sensitive to the range considered for  $\xi$ . Significant differences are also observed in the fracture locus obtained using different sets in the calibration. In this context, the fracture locus shape is also affected by the type of tests selected, within a similar range for  $\eta$  and  $\xi$ .

### 5.1.2. Analysis of the prediction ability

In this section, models' prediction ability is assessed based on the comparison of the relative errors between the predicted fracture strain and the one experimentally measured, for the 12 tests from #18 to 29#, carried out in the high  $\eta$  range (not considered for the models' calibration). Fig. 9 shows the relative error calculated for each test, considering the seven ductile fracture models calibrated using the different calibration sets.

Globally, Group 2 and 4 lead to similar distributions of the relative prediction error, which could be expected based on the analysis performed in the previous section. Groups 1 and 3 lead to similar levels of prediction accuracy, except for the X-W and H-C models, as shown in Fig. 9 (a) and (c), respectively. In fact, it is interesting to note that the M-W model is the only one presenting relative prediction errors lower than 50%, whatever the set adopted in the calibration procedure. Nevertheless, this is certainly related with its lower flexibility. On the other hand, the H-C model is the one presenting the higher sensitivity in the relative prediction error to the set used in the calibration procedure. In fact, when using Group 3, the H-C model is the one presenting the best prediction, followed by M-

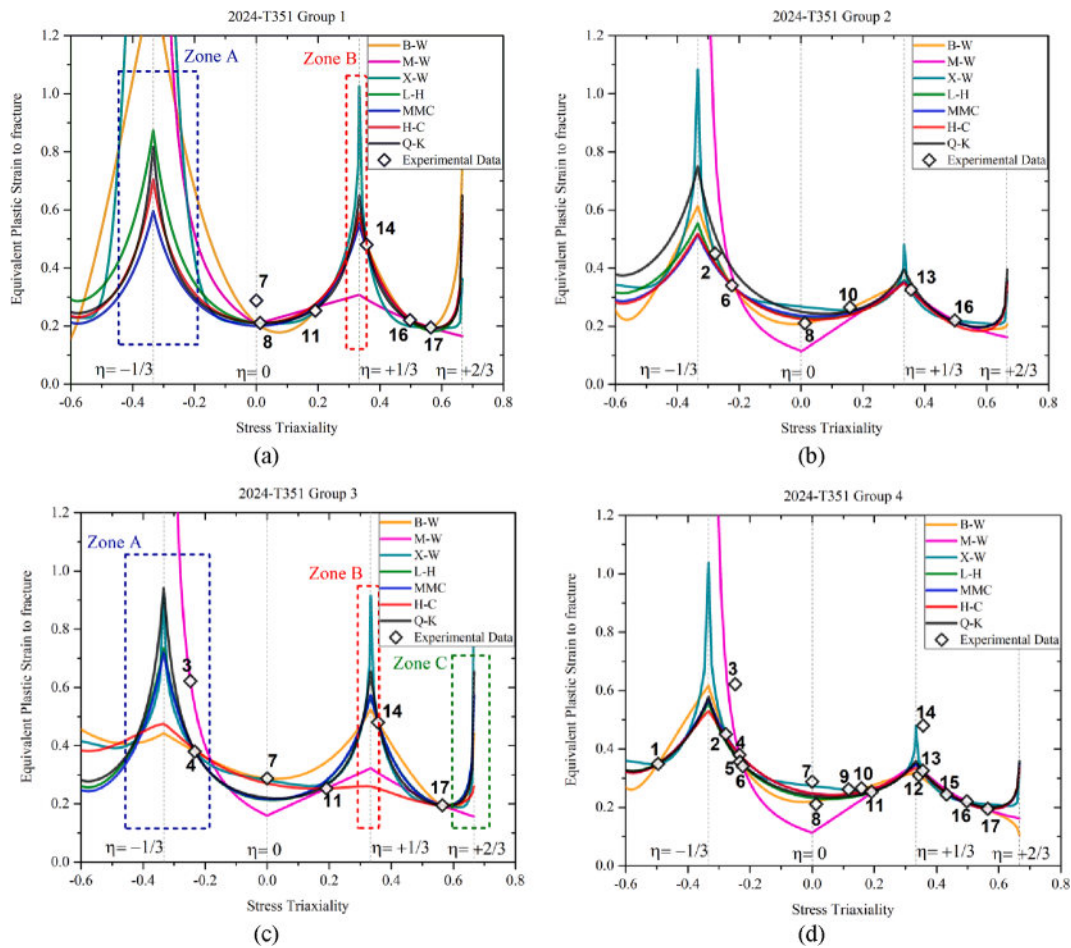


**Fig. 8.** Comparison of 2D fracture locus obtained with the seven uncoupled models for the 2024-T351: (a) Group 1; (b) Group 2; (c) Group 3; and (d) Group 4.

W model. All the other models fail to predict the fracture for the upper bound assumptions, i.e., for  $\xi = +1$ , when using Group 3. In this context, it is interesting to note that the type of tests seems to have a greater influence on the predictive ability than the range of stress states considered. In order to better understand the differences in the predictive ability of each model, when considering different sets in the calibration, the 3D fracture loci (plotted in the 3D space  $(\eta, \xi, \bar{\epsilon}_f)$ ) are also presented. Nevertheless, for each model, only the 3D fracture loci that lead to clearly distinct relative error predictions are shown, to simplify the discussion. In these figures, the 2D fracture locus is presented by the thick dash line, while the normalized uniaxial compression, plane strain, and uniaxial tension conditions are represented by the red, blue and black-coloured solid lines, respectively. The experimental tests used in the calibration procedure are marked with white-coloured diamonds. The tests performed under PSC, that were not included in the calibration procedure are marked by black-coloured circles. The tests used for the prediction accuracy, from #18 to #29, are displayed with the red-coloured circle marks. The fracture strain predicted for each test condition  $(\eta, \xi)$  defined in Table 1 is marked with blue-coloured circles. The relative errors for each test (#1 to #29) are denoted by black thin lines.

Regarding the B-W model, as previously mentioned, Groups 2 and 4 lead to quite distinct 2D fracture loci, particularly for the high range of  $\eta$ . Therefore, the shape of the 3D fracture loci is quite similar (concave shape), for low  $\eta$  values; but it becomes progressively flattened, for 2024-T351 Group 2, and a little convex, for 2024-T351 Group 4, at high  $\eta$  values (see zone C in Fig. 10 (b) and (c), respectively). The 3D fracture locus obtained with Group 3 has a concave shape for a wide range of  $\eta$  (Fig. 10 (c)). However, it is flattening out, for negative range of  $\eta$ . The 3D fracture locus is always concave when considering Group 1 (see Fig. 10 (a), respectively). It should be also mentioned that the calibration set also has a strong influence on the magnitude of the equivalent fracture strain, particularly in the lower and the upper bounds, i.e. for  $\xi = -1$  and  $\xi = +1$ .

Although the four calibration sets are based on distinct conditions, the shape of the fracture surface predicted by M-W model is quite similar. Therefore, Fig. 11 presents only the one obtained with Group 4. The fact that M-W model is  $\xi$ -independent and the existence of the cut-off value at the negative  $\eta$  limits its prediction capability (see also Fig. 9 (b)). Nevertheless, the magnitude of the fracture strains is slightly affected by the calibration set, as shown in Fig. 8.

Fig. 12 reveals some differences in the 3D locus shapes obtained with different calibration sets, for the X-W model. Note that groups



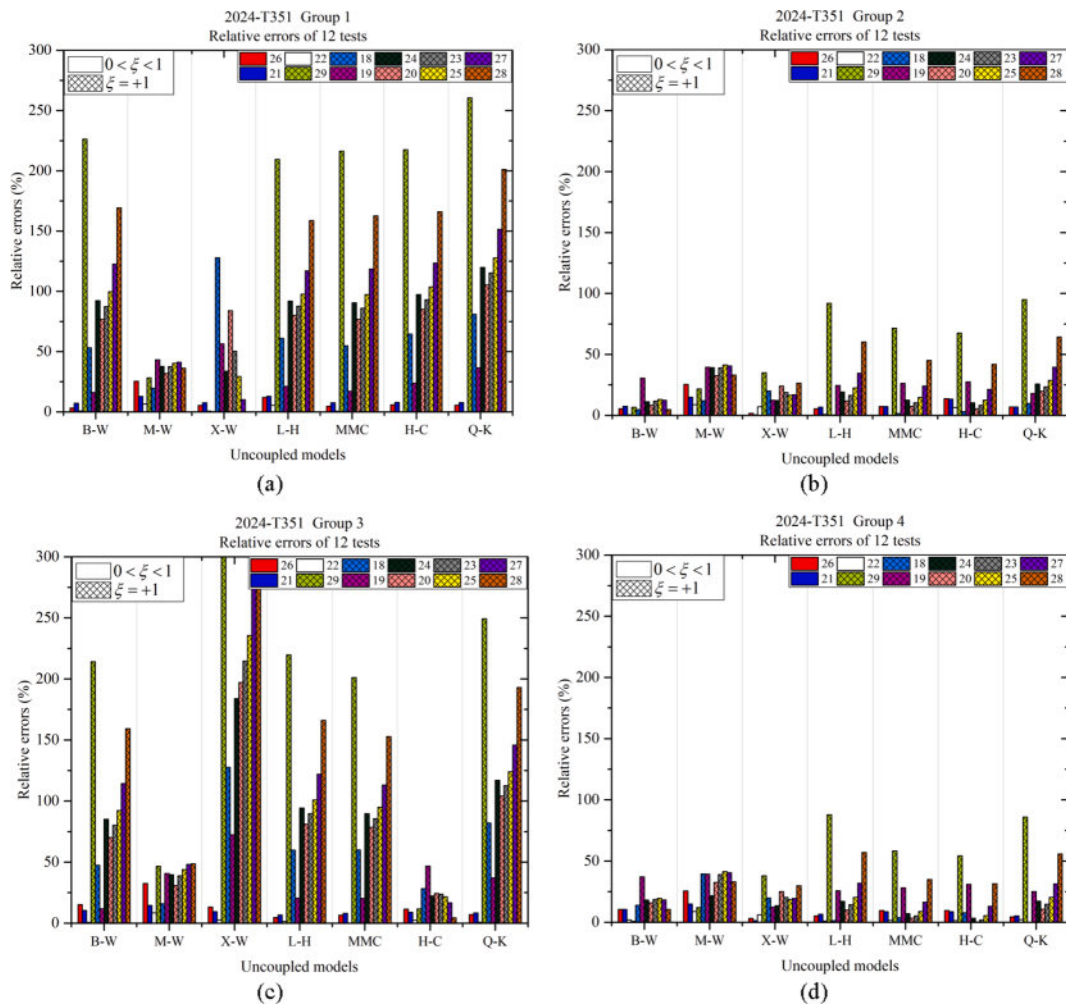


**Fig. 9.** Relative errors of fracture models prediction for the 12 tests #17- #29 using (a) 2024-T351 Group 1, (b) 2024-T351 Group 2, (c) 2024-T351 Group 3, and (d) 2024-T351 Group 4.

2 and 4 present similar trends of the 2D fracture loci and, consequently, also identical levels of prediction accuracy. Whatever the calibration set adopted, the 3D fracture loci of the X-W model has a concave shape for low  $\eta$  values. For high values, the shape changes; when Group 3 is adopted it remains concave, while it flattens out when using Group 4, and becomes convex when considering Group 1, (see zone C in Fig. 12). It is also interesting to note that, as for the B-W model, the calibration set also has a strong influence on the magnitude of the equivalent fracture strain, particularly in the lower and the upper bounds, i.e. for  $\xi = -1$  and  $\xi = +1$ .

Fig. 13 presents the 3D locus obtained for the H-C model, when using Group 1, 3 and 4. In this case, the bigger differences are observed when Group 1 is considered; i.e. the calibration procedure considers only tests in the positive range of  $\eta$ . As for B-W and X-W models, Group 1 leads to a concave fracture locus. The change of the calibration set results in the flattening out of the fracture locus, including for  $\xi = 0$ , and to a decrease of the fracture strain, particularly for  $\xi = \pm 1$  (see Fig. 13). Thus, the 3D fracture locus of the X-W, B-W and H-C models show high sensitivity to the type and number of tests used in their calibration, which leads to different prediction errors, as shown in Fig. 9. The comparative study of the MMC, L-H, H-C and Q-K models shows a similar level of prediction accuracy under different loading conditions, when considering different number of tests in their calibration procedure, i.e., Group 2 and 4, as previously shown in Fig. 5 and Fig. 9. These models, except H-C, also show quite similar results when adopting Group 1 and 3, as depicted by the average errors obtained with the 17 experimental tests in Fig. 5. Therefore, for the MMC, L-H and Q-K models the 3D fracture loci are presented only for Group 3 and 4, in Figs. 14, 15 and 16, respectively. The analysis of these figures shows that the 3D surface of these models is quite similar when the calibration is performed with the 6 experimental tests, considered in Group 3; it presents always a concave shape. For MMC, L-H and Q-K models, the usage of a large number of tests (17 tests) leads to a shift of the boundary curves corresponding to  $\xi = -1$  and  $\xi = +1$  downwards, as shown in Figs. 14, 15 and 16, respectively. Moreover, their global shape is flatter.

The analysis of region D (see Fig. 14 (b)), confirms that the B-W, MMC, and H-C models show the more accurate predictions at  $\xi = +1$ , when using Group 4. In contrast, L-H and Q-K models have higher average prediction errors in the high  $\eta$  range. In fact, in this

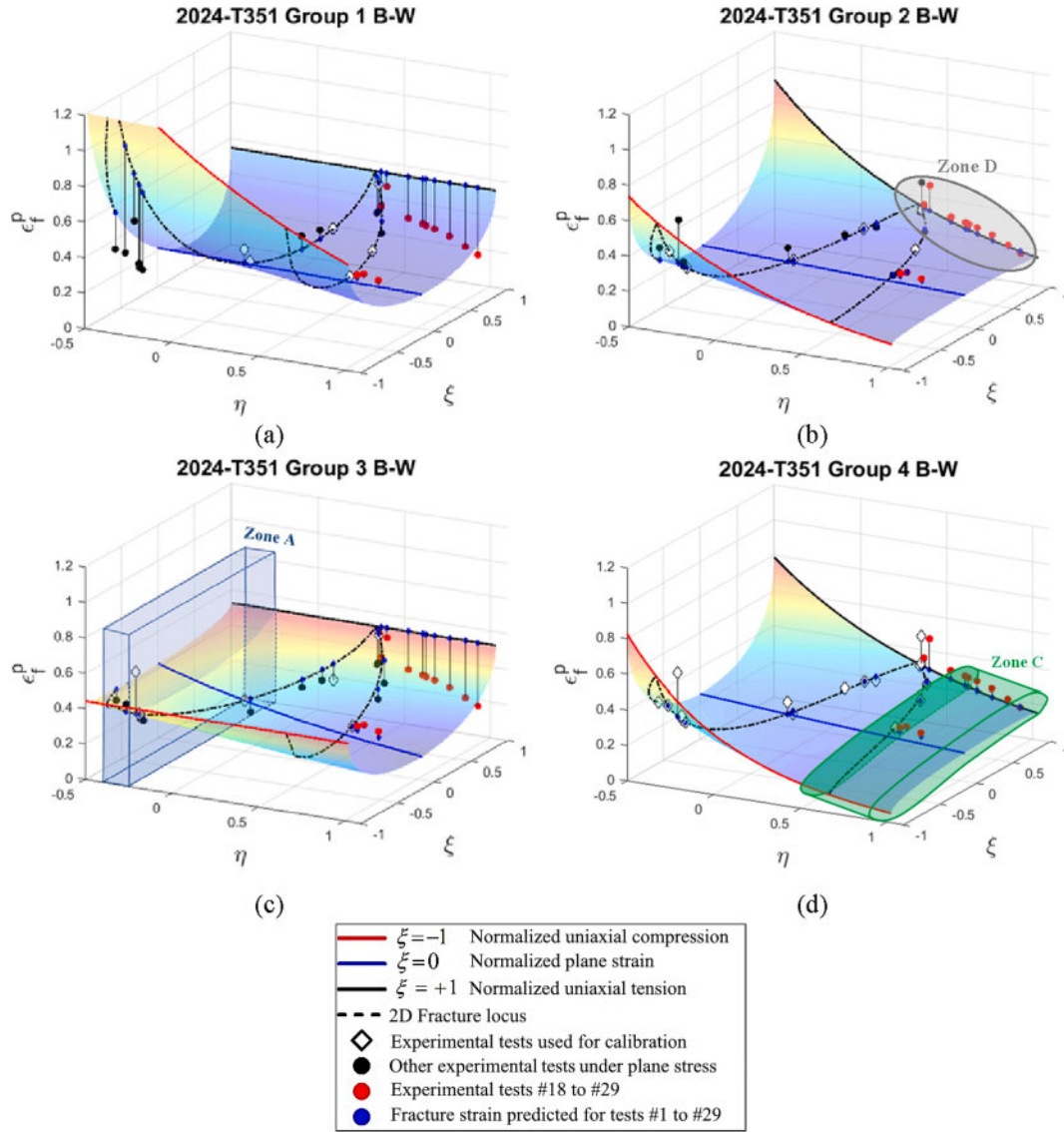


**Fig. 10.** 3D fracture loci obtained for the B-W model considering different sets of tests in the calibration procedure performed for the 2024-T351 aluminium alloy: (a) Group 1; (b) Group 3; (c) Group 3 and (d) Group 4.

range, it is found that the effect of  $\xi$  on the 3D fracture loci predicted by these models becomes very weak, especially for  $\eta \geq 0.5$  (see Zone C, as depicted in Fig. 10 (c)).

In summary, the comparative study on ductile fracture prediction for the 2024-T351 aluminium alloy shows that the B-W model provides the best prediction accuracy, followed by X-W, MMC and H-C models. These models show a very similar level of prediction accuracy when using sets with different number of tests, i.e., Group 2 and 4. Moreover, L-H and Q-K models show satisfactory results in the negative and low- $\eta$  ranges, but they fail to predict the fracture in normalized uniaxial tension. Other studies have shown that Q-K model is unable to predict failure under tension, although the authors state that its development is based on the mechanisms of nucleation, void growth and coalescence ([31,72]).

The results obtained with the calibration performed using Group 1, which includes only tests in the positive  $\eta$  range, exhibits a similar level of prediction for X-W and M-W models, followed by B-W, MMC, L-H and H-C models. When using Group 3 in the calibration the H-C model shows the best prediction, followed by M-W model. It can be concluded that the different types and number of tests used in the models' calibration have an influence on the shape of the 3D fracture locus, particularly its boundary curves, corresponding to  $\xi = -1$ ,  $\xi = 0$  and  $\xi = +1$ . Consequently, they have a strong impact on the prediction accuracy of models, except for the M-W model, due to its poor flexibility.

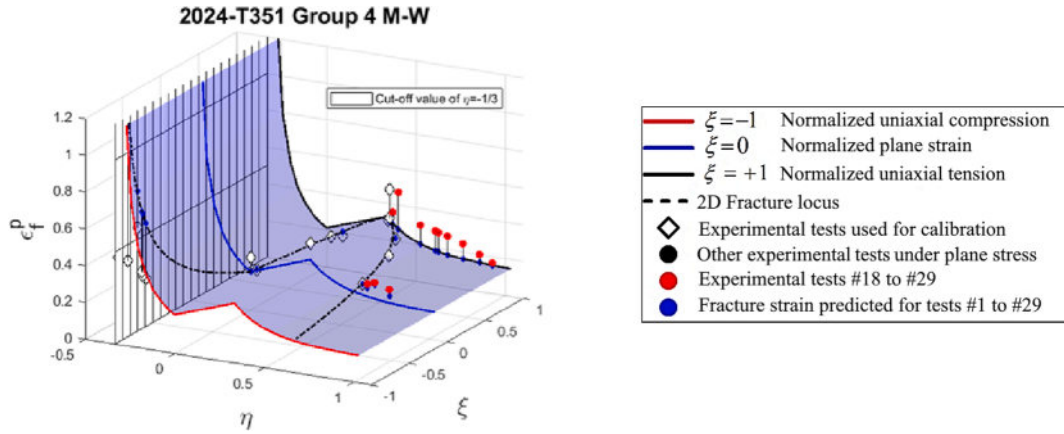


Fig. 11. 3D fracture loci obtained for the M-W model for the 2024-T351 aluminium alloy when using Group 4.

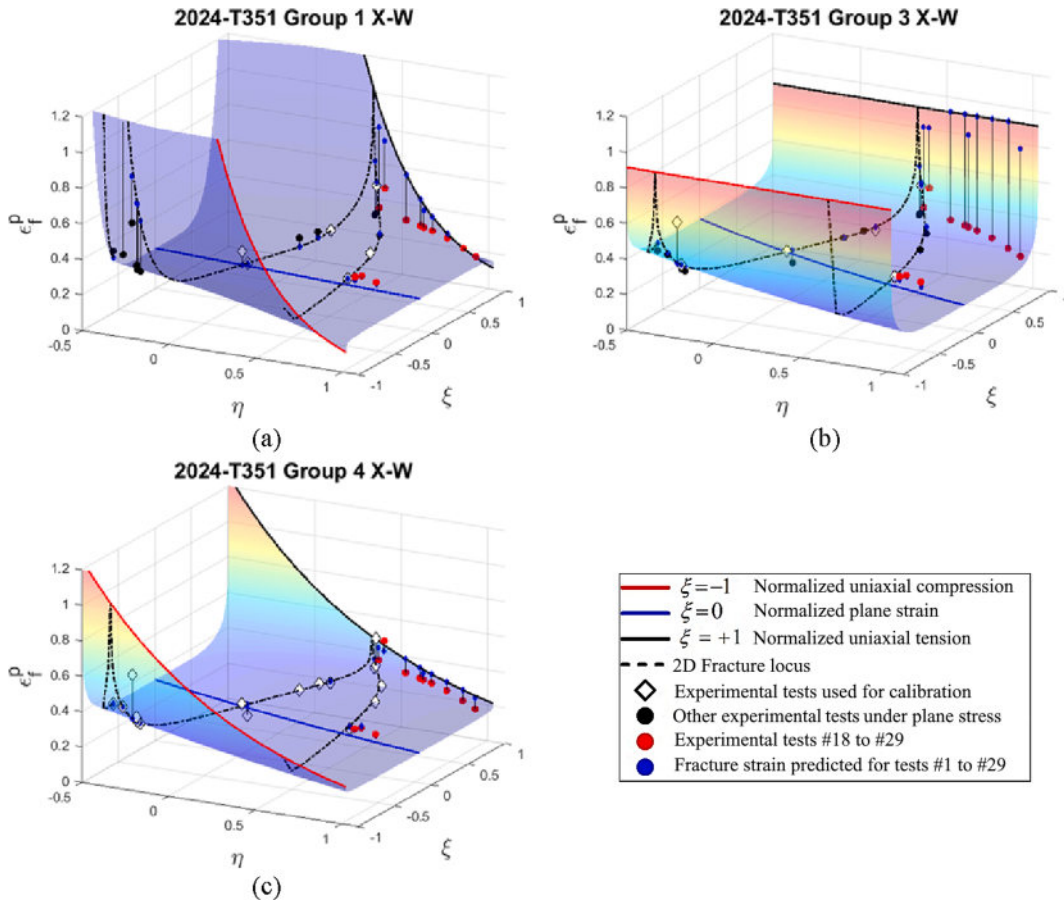


Fig. 12. 3D fracture loci obtained for the X-W model considering different sets of tests in the calibration procedure performed for the 2024-T351 aluminium alloy: (a) Group 1; (b) Group 3 and (c) Group 4.

### 5.1.3. Comparative study with previous works

Some of the fracture models selected have been calibrated and evaluated in previous studies, also using the experimental data available for the 2024-T351. In this context, it is interesting to shed some lights on the similarity and the fundamental disagreement between the current work and the previous works, where the calibration procedures used the, as will be shown in the following.

The parameters of the MMC, H-C and L-H models were calibrated, using the least square method, applied to the same 17 experimental tests used in Group 4. The trends of the fracture locus obtained as well as the average calibration errors are very similar to the



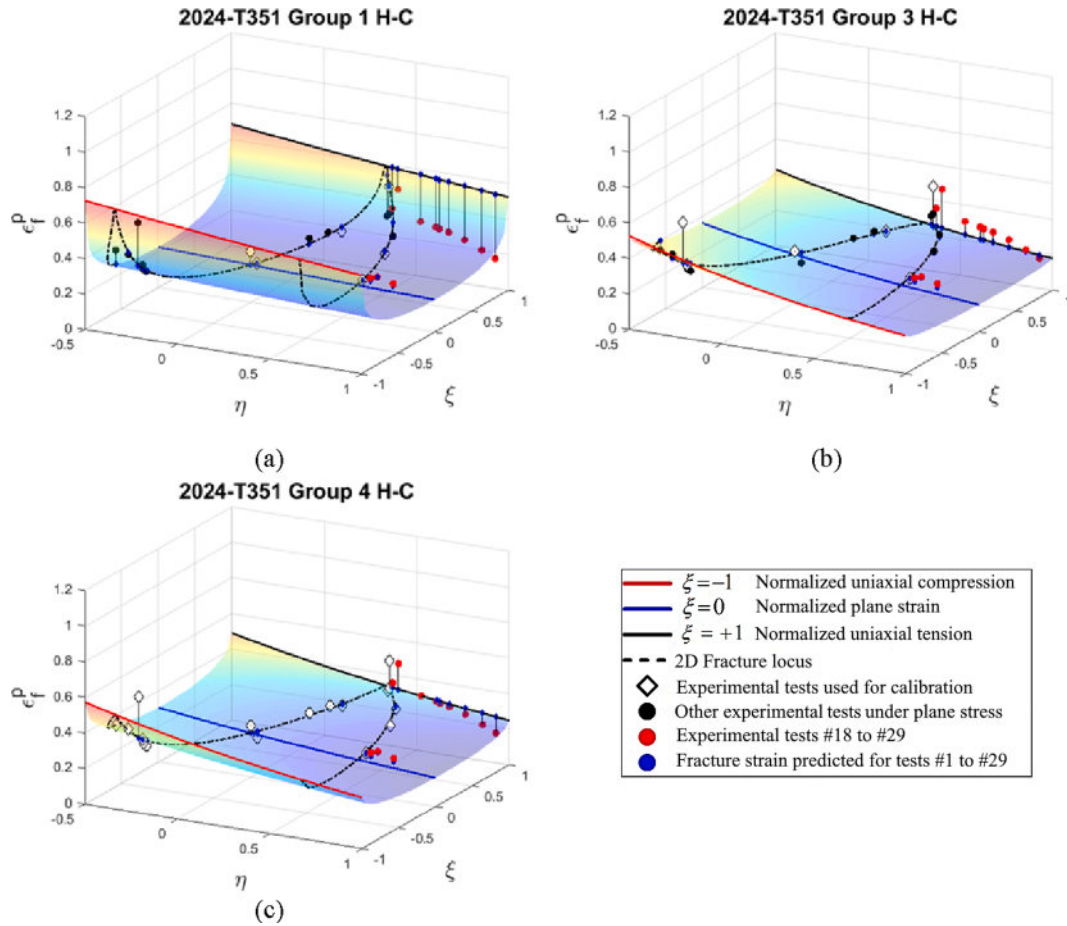


**Fig. 13.** 3D fracture loci obtained for the H-C model considering different sets of tests in the calibration procedure performed for the 2024-T351 aluminium alloy: (a) Group 1; (b) Group 3 and (c) Group 4.

ones reported in this study. Nevertheless, the predictive ability is quite different for tests #19, #20, #22, #24 and #28; it is better in the current study for tests #20, #22 and #24 and worst for tests #19 and #28, which can be related with the different methodology adopted to solve the non-linear problem [8]. The Q-K and MMC models were also calibrated and compared with the L-H one (see details in [54]) by Quach et al. [9]. In this case, a set of 18 tests was used in the calibration procedure, by adding to the 17 tests, considered in Group 4, the tensile test on a flat grooved specimen (test #21) (see Table 1). Note that Group 4 leads to a good prediction of this test, which is not considered in the models' calibration (see Fig. 9 (d)). The results obtained with 18 tests present a shift of the 2D fracture locus upwards, particularly for the local peaks corresponding to  $\eta = -1/3$  and  $\eta = +1/3$ , when compared with the results obtained for Group 4; in both studies the results for the three uncoupled models are quite similar. This shift corresponds to a lower relative error for tests #3 and #14 than the one obtained in this work with Group 4. By contrast, the relative errors of the tests #2, #4, #5, #6, #12 and #13 predicted with Group 4 are lower, for L-H and MMC models. For Q-K model, only the relative errors corresponding to tests #12 and #13 obtained with Group 4 are lower than the ones reported in [9]. The shape of 3D fracture loci is similar for normalized uniaxial tension, but it becomes different for normalized uniaxial compression, which corroborates the impact of the method selected to solve the non-linear problem. In another study, the X-W and MMC models were calibrated using 12 tests, corresponding to the range from  $-0.278$  to  $0.603$  for  $\eta$  and to the range from  $-0.969$  to  $0.99$  for  $\xi$  [26]. Note that this set includes two tests (#18 and #21) that were not included in the current study, while it discards tests #1, #7, #10, #11, #15, #16 and #17 (see Table 1). Compared with Group 4, the set of 12 tests has a similar range for  $\xi$  and a slightly lower range for  $\eta$ . The damage parameters and the shape of 3D fracture loci obtained with this set for MMC model are similar to the ones obtained with Group 4. For the X-W model, although the shape of the 3D fracture locus obtained with 12 tests and Group 4 is quite similar for the negative range of  $\eta$ , it becomes different (convex shape for the calibration with 12 tests, as occurs in the current study for Group 1 (see Fig. 10 (a)), for positive high  $\eta$  values ([2,26]). These results confirm that more flexible models are more sensitive to the type and number of tests considered in calibration. Finally, the B-W model was also calibrated using the same type of tests using a methodology based on the separate identification of the damage parameters for each of the three boundary curves, i.e.,  $\xi = -1$ ,  $\xi = 0$  and  $\xi = +1$  ([32,35]). The set used consists of 15 tests, ten coincident with the ones used in Group 4 (tests #2 - #6, #8, #9 and #12 - #14) and other 4 that were not (tests #18, #19, #21, #24 and #29). This corresponds to a range for  $\eta$  from  $-0.278$  to  $0.93$  and for  $\xi$  between  $-0.91$  and  $1$ . As results, the

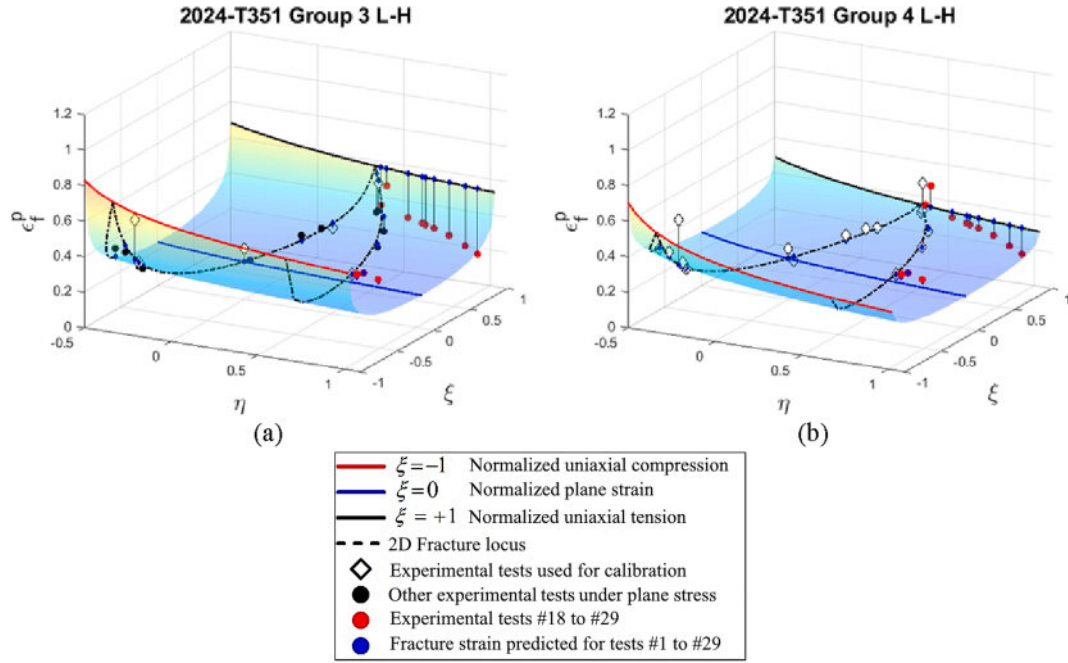


**Fig. 14.** 3D fracture loci obtained for the L-H model considering different sets of tests in the calibration procedure performed for the 2024-T351 aluminium alloy: (a) Group 3 and (b) Group 4.

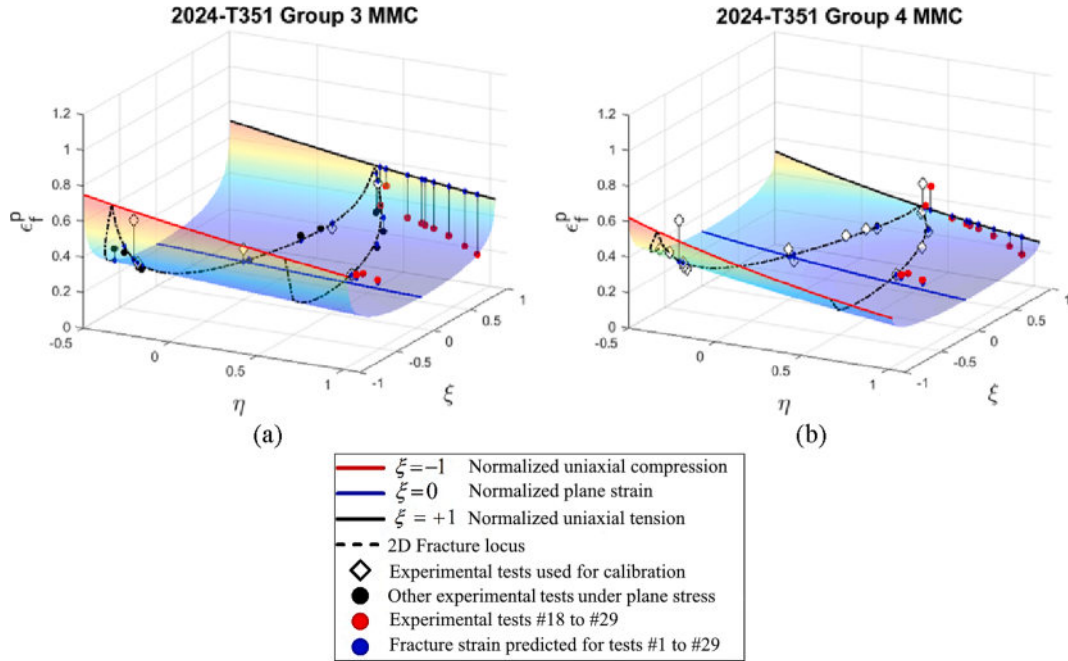


**Fig. 15.** 3D fracture loci obtained for the MMC model considering different sets of tests in the calibration procedure performed for the 2024-T351 aluminium alloy: (a) Group 3 and (b) Group 4.

shape of 3D fracture surface obtained with 15 tests in the calibration seems very similar to the 3D fracture locus obtained with Group 2 and 4, for  $\xi = 0$  and  $\xi = +1$ , but it becomes a slightly different at  $\xi = -1$ , for the negative values of stress triaxiality. This shows that not only the number and type of tests has an impact on the calibration of B-W model but also the methodology considered in the optimization process.

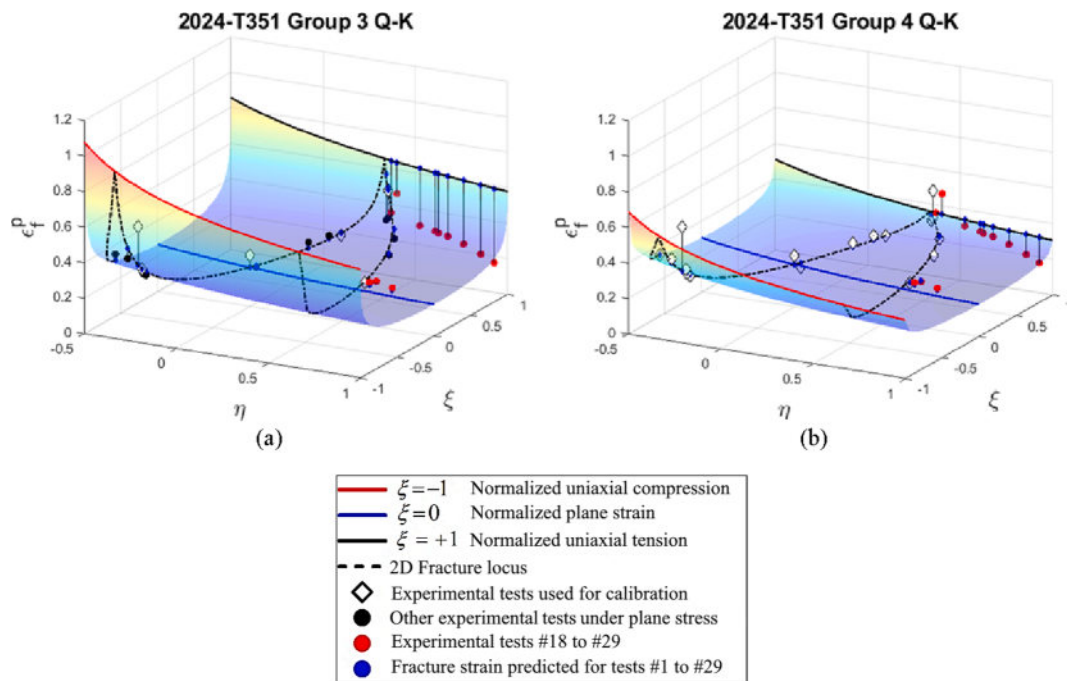


**Fig. 16.** 3D fracture loci obtained for the Q-K model considering different sets of tests in the calibration procedure performed for the 2024-T351 aluminium alloy: (a) Group 3 and (b) Group 4.

## 5.2. Analysis of the fracture models for DP600 steel

### 5.2.1. Analysis of the calibration error

Table 5 lists the ductile fracture parameters obtained for the seven models selected, for DP600. Fig. 17 shows the percentage average calibration error calculated using Eq. (39), at the convergence of the models' calibration procedure. All models lead to a very

**Table 5**  
Damage models parameters identified using DP600 steel.

Model	Damage Parameters	
	Parameters	DP600 steel
B-W	$D_1$	0.9653
	$D_2$	0.0002
	$D_3$	0.9036
	$D_4$	0.9677
	$D_5$	1.4999
	$D_6$	0.8784
M-W	$D_1$	0.84
	$D_2$	2.086
	$D_3$	-3.703
	$D_4$	0.3577
X-W	$C_1$	1.5791
	$C_2$	1.0
	$C_3$	0.9671
	$C_4$	0.8866
L-H $C = 1/3$	$c_1$	4.0985
	$c_2$	1.2510
	$c_3$	0.9821
MMC	$c_1$	0.1
	$c_2(\text{MPa})$	505.956
H-C	$c_3$	0.9639
	$a$	1.0961
	$b$	0.9753
Q-K	$c$	0.1053
	$C_1$	1.9052
	$C_2$	1.5006
	$C_3$	3.3479

similar value of the average calibration error, lower than 12%, except the M-W.

Fig. 18 shows the relative calibration error, calculated for each of the 6 tests considered in the calibration (tests #1 to #6 for DP600 steel, in Table 2), which corresponds to the gap between the experimental fracture strain and the one predicted by the model. For this material, all models are unable to capture the ductile fracture for the pure shear test (test #2), combined shear-tension test (test #3), and Nakazima test (test #6). The 2D fracture locus obtained with the seven uncoupled ductile fracture models are presented in Fig. 19. All models, except M-W, describe the decrease of the fracture strain with the decrease of the triaxiality from  $-0.6$  to  $-1/3$ . As previously mentioned, this exception noticed for the M-W model is related with the fact that this model imposes a cut-off value for  $\eta = -1/3$ . All describe the increase of the fracture strain with the decrease of the triaxiality from  $-1/3$  to  $0$ . For the low range of positive stress triaxiality ( $0 \leq \eta \leq 1/3$ ), the material ductility predicted sharply decreases as a function of the increase of  $\eta$  and then it increases rapidly until the  $\eta$  reaches  $1/3$ . In the high range of positive stress triaxiality ( $\eta \geq 1/3$ ), the fracture strain starts to decrease and then, increases until the  $\eta$  reaches approximately  $2/3$ . In fact, all models except M-W, display an asymptotic behaviour close to  $\eta = +2/3$ , under PSC. Nevertheless, this is not enough to capture the Nakazima test (test #6;  $\eta = 0.66$ ) fracture strain, leading to errors higher than 15% for all models, as shown in Fig. 18. Fig. 19 also highlights that L-H, MMC, H-C and Q-K lead to similar 2D fracture locus for  $\eta \geq -1/3$  (see also the average calibration error in Fig. 17).

### 5.2.2. Analysis of the prediction ability

For DP600 steel, the experimental tests considered for evaluating the prediction accuracy are the ones from #7 to #18, in Table 2. These 12 tests were carried out in the high  $\eta$  range. Fig. 20 shows the relative prediction errors of the seven ductile fracture models. It is clear that all models are not able to predict the fracture strain for the tensile test performed on a Grooved flat, with  $R = 2$  mm (test #13), and with  $R = 4$  mm (test #12), and for the smooth flat subjected to tension (test #7). Moreover, all models lead to similar relative error values for all the tests with  $\xi = 0$ . On the other hand, the X-W, L-H and Q-K models present also a similar level of prediction accuracy for the tests with  $\xi = +1$ .

The 3D fracture loci obtained for the DP600 steel are presented in Fig. 21. In this figure, the 2D fracture locus is displayed by the thick dash line, whereas the normalized uniaxial compression, plane strain, and uniaxial tension conditions are represented by the red, blue and black-coloured solid lines, respectively. The six experimental tests used for the calibration procedure, from #1 to #6, are marked with white-coloured circles. The tests used for the prediction accuracy, from #7 to #18, are displayed with the red-coloured circle marks. The fracture strain predicted for each test condition ( $\eta, \xi$ ) defined in Table 2 is marked with blue-coloured circles. The relative errors for each test (#1 to #18) are denoted by black thin lines. For this material, the B-W model leads to a quite flat surface while the ones obtained by MMC and H-C are quite similar. Nevertheless, for the high range of  $\eta$  the surfaces present a quite similar trend for all models. Therefore, Fig. 21 shows that all ductile fracture models, except the B-W, underestimate the fracture strain of the experimental tests considered in the evaluation of the prediction ability.

### 5.3. Comparative analysis of the models' calibration and prediction tendencies for the two materials

As previously mentioned, the set of experimental tests considered for the DP600 presents a range for the  $\eta$  identical to the one of Group 1 for the 2024-T351, but a wider range for  $\xi$ . On the other hand, when compared with Group 2 for the 2024-T351, the range for  $\xi$  is identical while the range for  $\eta$  is narrower.

Comparing the average calibration errors obtained for 2024-T351 with Group 1 (Fig. 8, grey bars) and DP600 (Fig. 17), it is shown that they are identical for both materials (lower than 14%), meaning that the fracture strain values are globally well described for both materials. Nevertheless, for the 2024-T351, a smaller average calibration error is obtained, particularly for B-W, X-W and Q-K models.

If the comparison is made for 2024-T351 calibrated with Group 2 (Fig. 8, yellow bars) the difference between both average calibration errors becomes slightly bigger, because it has smaller values than the one obtained with Group 1, except for M-W and Q-K. These results indicate that the average calibration error can be improved by considering a wider range for  $\xi$ , but this depends also on the type of tests selected, as previously discussed when analysing the influence of the calibration sets. As previously mentioned, for the DP600 steel, none of the models are able to accurately capture the fracture strain for the pure shear test (test #2) and the combined shear-tension test (test #3), which present a conflicting trend. The same effect is observed for the 2024-T351 calibrated with Group 3, when compared with Group 2.

Regarding the 2D fracture locus obtained for 2024-T351 (Fig. 8 (a) and (b)) and DP600 steel (Fig. 19), the results show that the predicted equivalent strains at fracture for the 2024-T351 aluminium alloy are much lower than those obtained for DP600 steel, as expected from the experimental results shown in Table 1 and Table 2. It is also noticed that the fracture models present quite different trends for both materials, particularly in the low range of positive stress triaxiality ( $0 \leq \eta \leq 1/3$ ), when the comparison is made with Group 1, for the 2024-T351. On the other hand, the trend becomes more similar when considering Group 2, for the 2024-T351 (Fig. 8 (b)), highlighting the impact of the fracture strain considered for  $\eta$  close to  $1/3$ . In contrast to the fracture locus obtained for 2024-T351 Group 1 (Fig. 8 (a)), for DP600 steel (Fig. 19), the fracture strain predicted by all the models exhibits an inflection point for a  $\eta$  close to  $0.2$ . This behaviour was also observed for the 2024-T351, for some models, when using Group 3 (see Fig. 8 (c)), which once again highlights the importance of the experimental tests selected. Moreover, the X-W and B-W models also present quite different trends for  $\eta = -1/3$  (see Fig. 8 and Fig. 19), for both materials. For DP600 steel, the fracture strains obtained with X-W and B-W models are lower than the ones predicted by the other models, for  $-1/3 \leq \eta \leq 0$ . However, for 2024-T351 calibrated using Group 1, the fracture locus predicted by these two models are much higher than the ones corresponding to L-H, H-C, and Q-K models, particularly in the negative range of  $\eta$ . The differences observed between the fracture strains predicted by X-W and B-W models, when compared with the other models, can be explained by the lack of experimental data points in this range. This could have an impact on the accuracy of the

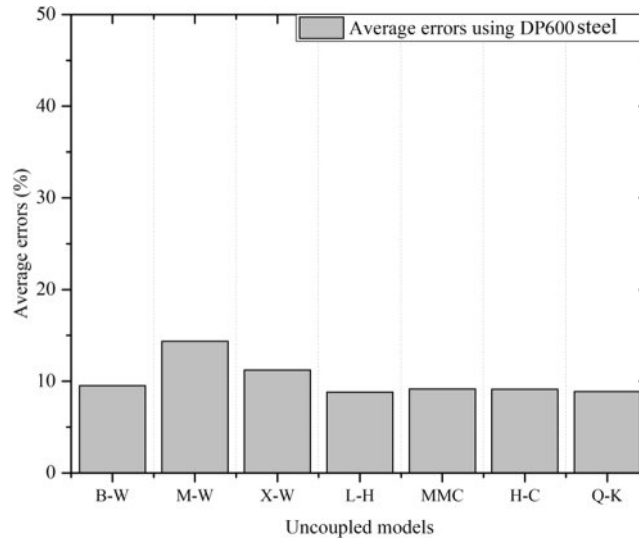


Fig. 17. Average errors predicted in the calibration procedure for the DP600 steel.

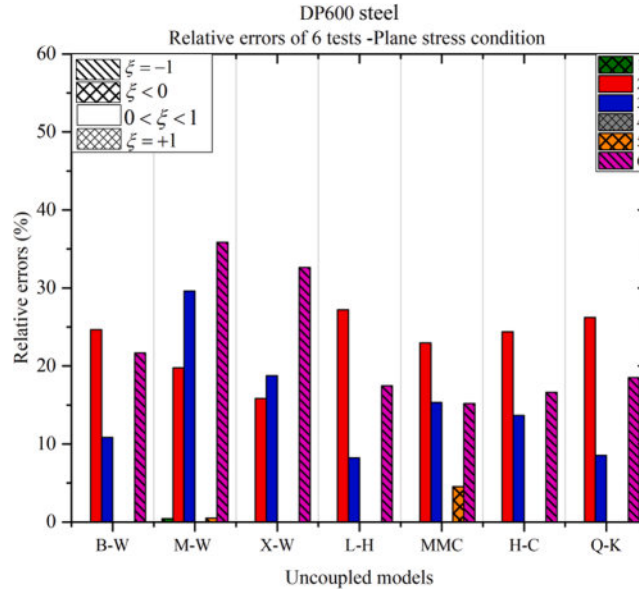


Fig. 18. Relative errors of fracture models obtained in the calibration procedure under PSC for DP600 steel.

calibration procedure, particularly for X-W and B-W models, which are more flexible than the others. Moreover, for 2024-T351 calibrated using Group 1, the X-W model shows high magnitude of the fracture strain for  $\eta = +1/3$  (zone B in Fig. 8 (a)). This is likely a result from the elliptic function used to describe the drop of material ductility due to the influence of  $\xi$ , but also a consequence of the high value of fracture strain associated to test #14.

The percentage average errors associated to all the tests used in the prediction accuracy (tests #7 to #18, for DP600 steel and #18 to #29, for 2024-T351), and the ones obtained from both the calibration and the evaluation of the prediction ability (tests #1 to #18, for DP600 steel, and #7, #8, #11, #14, #16, #17 and from #18 to #29, for 2024-T351 calibrated using Group 1; and #2, #6, #8, #10, #13, #16 and from #18 to #29, for 2024-T351 calibrated using Group 2) are shown in Fig. 22. From these results, it is interesting to note that the X-W model is the only one presenting similar average prediction errors for both materials, when Group 1 is adopted in the calibration procedure, which are among the lowest ones. However, the 2D fracture locus are quite different for both materials (see Fig. 8 (a), (b) and 19 (c), respectively). Fig. 22 highlights that for the DP600 steel, the B-W and X-W models present more accurate prediction than the others models, for the tests from #7 to #18. On the other hand, there are slightly differences in the average error values of the seven selected models when considering all tests (see white-coloured bars). For the 2024-T351 aluminium alloy, when considering Group 1, the M-W and X-W models present clearly lower values of average prediction errors than the other models (see



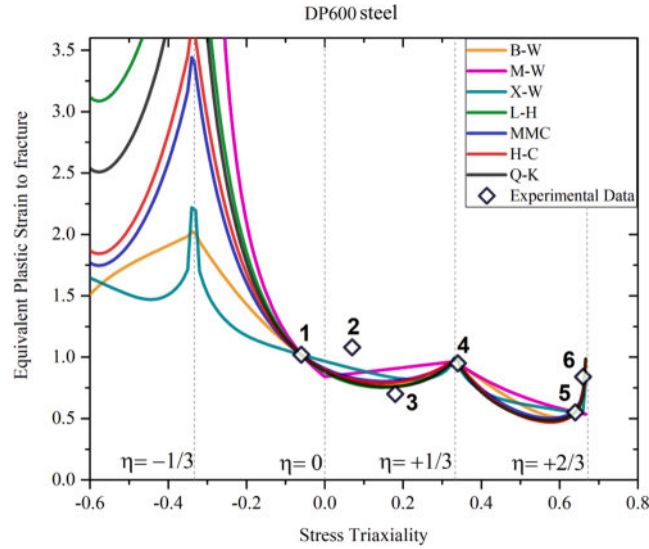


Fig. 19. Comparison of 2D fracture locus obtained with the seven uncoupled models for DP600 steel.

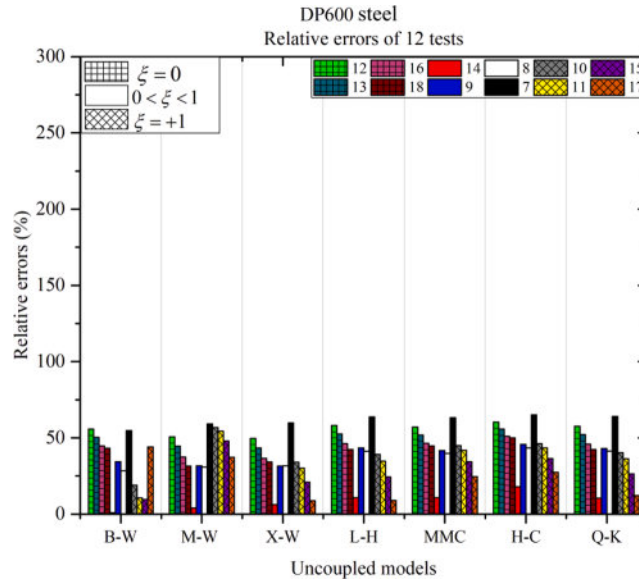


Fig. 20. Relative errors of fracture models prediction for the 12 tests from #7 to #18 for DP600 steel.

medium grey dashed bars, in Fig. 22). The highest average prediction error values obtained for this material can be explained by the fact that all the models, except M-W and X-W, are not able to properly predict the fracture strain for the upper bound assumption (i.e.,  $\xi = +1$ ), particularly, for smooth and small notched bars subjected to tension (tests #20 and #29) (see Fig. 9 (a)). For DP600 steel, Fig. 20 shows that all the models describe slightly better the fracture prediction at the tests corresponding to  $\xi = +1$  than for the 2024-T351 aluminium alloy, calibrated with Group 1. Nevertheless, when the comparison is made with the calibration performed using Group 2 for the 2024-T351 aluminium alloy, one can see an opposite trend.

Regarding the 3D fracture locus obtained for 2024-T351 Group 1 (Figs. 10-16), the results show that all models overestimate the experimental tests for  $\xi = +1$ , except for the M-W model. The adopting of Group 2 only changes this trend for the B-W model. However, for the DP600 steel, all models, except B-W, underestimate the tests corresponding to  $\xi = +1$ , as shown in Fig. 21.

## 6. Conclusion

A comparative study on the effect of the type and number of tests used for the calibration of seven ductile fracture models on their capability to forecast the failure behaviour of the 2024-T351 aluminium alloy and DP600 steel was presented. The calculated error

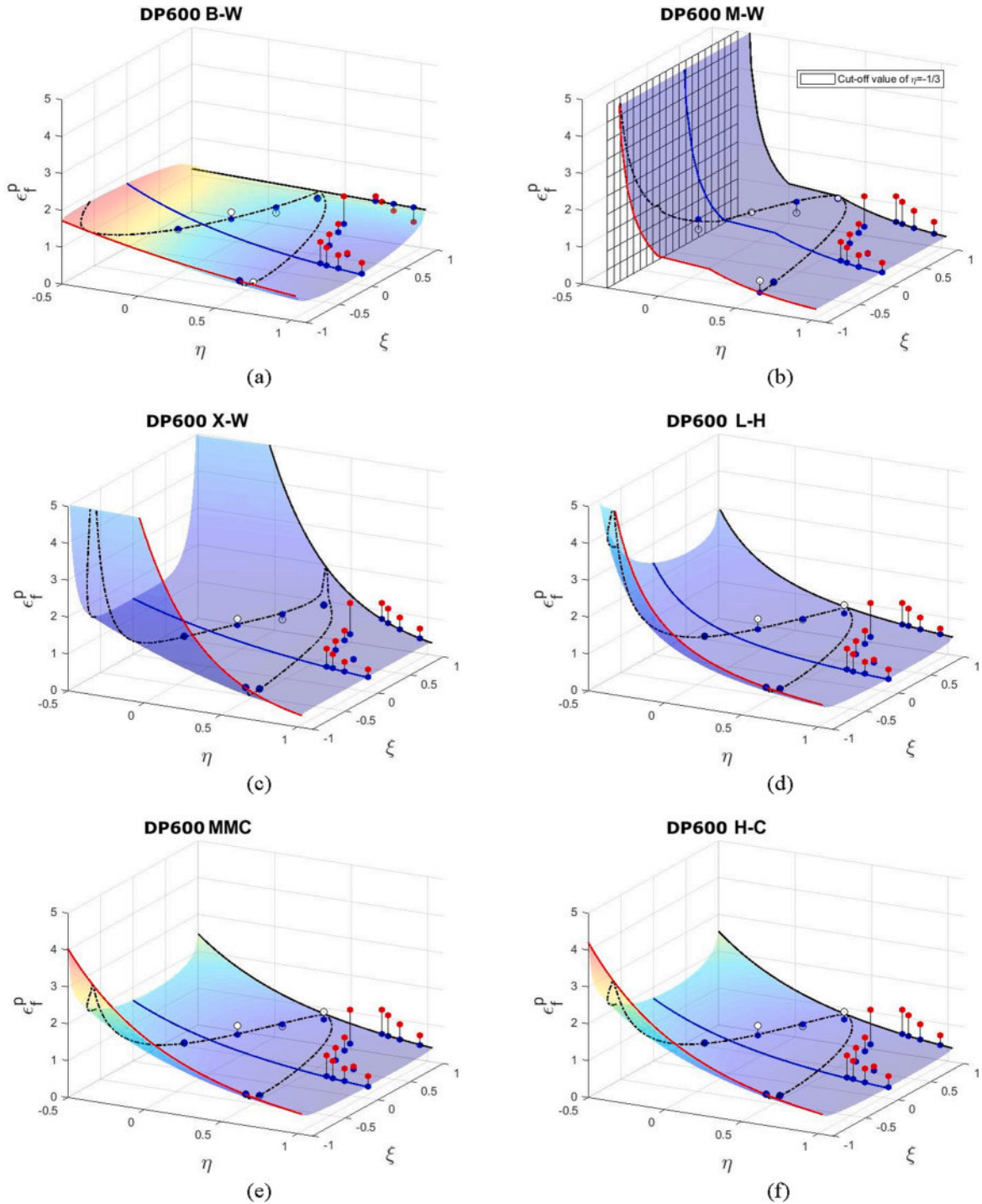


**Fig. 21.** 3D fracture loci obtained for the: (a) B-W, (b) M-W, (c) X-W, (d) L-H, (e) MMC, (f) H-C and (g) Q-K models calibrated for the DP600 steel.

between the predicted and the experimental fracture strains allows to assess both the prediction performance of the calibrated models and, consequently, the adequacy of the chosen experimental dataset used for models' calibration. It is noteworthy, that the available experimental data was split in two subsets, for both materials. The first one includes tests that were carried out under PSC. The second subset was not used in the models' calibration, but in the assessment of the ability of the calibrated models to forecast ductile failure. For the 2024-T351, the set of tests performed under PSC was divided into three subsets of 6 tests, which covering some chosen stress



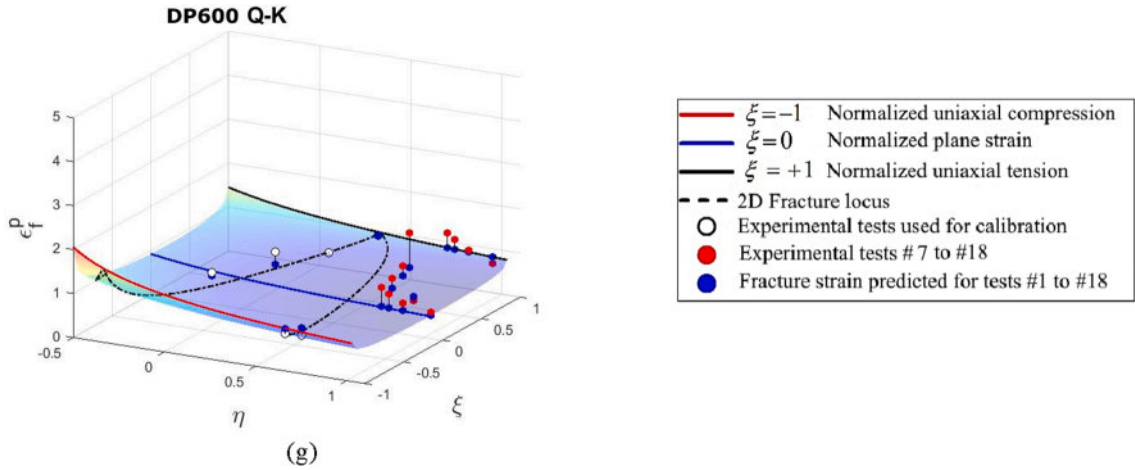


Fig. 21. (continued).

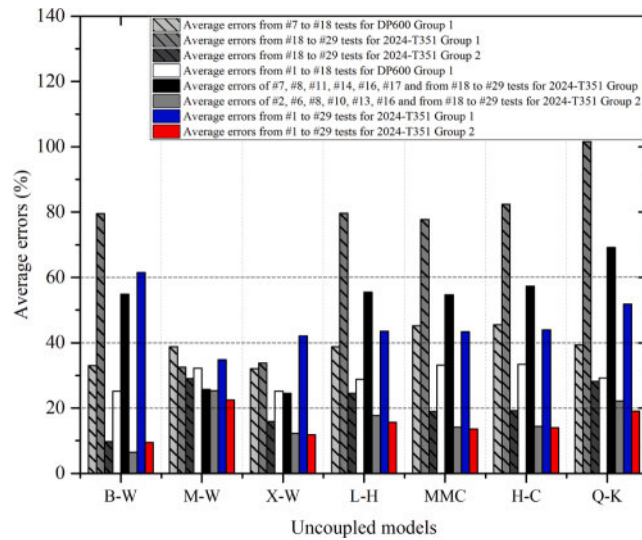


Fig. 22. Average errors of fracture models for all the tests used in the calibration and prediction for DP600 steel and 2024-T351 aluminium alloy (Group 1 and Group 2).

states. Based on the analysis of the obtained results, the main conclusions are drawn below.

For 2024-T351 aluminium alloy, it was shown that different types and numbers of tests, lead to distinct calibration results; but low average prediction errors are found for the more flexible models. In fact, these models present similar average prediction errors when calibrated with 6 or 17 tests, covering a similar range for the variables that characterize the stress state and fracture strain values. It was also noticed that low models' predictivity nearby the specific stress triaxiality values of  $\eta = -1/3$  and  $\eta = +1/3$  ("angular points" or cut-off for M-W model for  $\eta = -1/3$ ), for which the fracture strain predicted is quite sensitive to the type of tests selected. Therefore, the design of specific experimental tests for which the stress triaxiality are nearby these critical values is desirable.

The calibration of the fracture models using the DP600 steel experimental dataset, which is more restrictive than the one available for 2024-T351, was performed in an attempt to generalize the tendencies of the calibration and verification procedures achieved for the aluminium alloy. Indeed, it was shown that accurate results in the calibration procedure and in the prediction ability can be obtained when the experimental set used in the calibration covers a range as wide as possible of both the stress triaxiality and the Lode parameter. The range covered for the Lode parameter is particularly critical for the more flexible models. For the materials under analysis, the X-W model seems to be the one leading to a more accurate description of all tests.

It was shown that an experimental set of at least 6 tests is sufficient for an accurate calibration of the most flexible uncoupled models and similar calibration and verification results may be achieved, with what it is obtained using 17 tests. This involves choosing experimental tests for the calibration procedure that cover a wide range of stress states. Thence, when the calibration procedure is applied using a similar range for  $\eta$  and a wider range for  $\xi$ , the average calibration errors obtained for all models tend to reduce. Last

but not least, the use of some experimental tests characterized by identical values of stress triaxiality and Lode parameter, but different fracture strains, can be detrimental for the calibration procedure. The origin for this discrepancy in the experimental fracture strain value can be related, among other sources, with the uncertainty on the location and measurement of the principal strains, the quality of the machined samples, the heterogeneity and scattering of the material properties, etc. In this context, the use of the same type of specimens (e.g. plate or tubular) can help reducing some sources of scattering. Nevertheless, it will be profitable to use probabilistic approaches that can handle different sources of scattering to develop robust calibration procedures.

### CRedit authorship contribution statement

**Mariem Noura:** Writing – review & editing, Writing – original draft. **Marta Cristina Oliveira:** Conceptualization, Formal analysis, Visualization, Resources, Software, Supervision, Writing – review & editing. **Ali Khalfallah:** Writing – review & editing, Supervision. **José Luís Alves:** Resources, Software. **Luís Filipe Menezes:** Resources, Software.

### Declaration of Competing Interest

The authors declare that they have no known competing financial interests or personal relationships that could have appeared to influence the work reported in this paper.

### Data availability

Data will be made available on request.

### Acknowledgements

The authors gratefully acknowledge the financial support of the Portuguese Foundation for Science and Technology (FCT) under the projects with reference 2022.08459.PTDC, UIDB/00285/2020 and LA/P/0112/2020.

### References

- [1] Bao Y. Prediction of Ductile Crack Formation in Uncracked Bodies. PhD thesis, Massachusetts Institute of Technology; 2003.
- [2] Wierzbicki T, Bao Y, Lee YW, Bai Y. Calibration and evaluation of seven fracture models. *Int J Mech Sci* 2005;47(4-5):719–43. <https://doi.org/10.1016/j.jimecsci.2005.03.003>.
- [3] Rice JR, Tracey DM. On the ductile enlargement of voids in triaxial stress fields\*. *J Mech Phys Solids* 1969;17(3):201–17. [https://doi.org/10.1016/0022-5096\(69\)90033-7](https://doi.org/10.1016/0022-5096(69)90033-7).
- [4] Tvergaard V. Influence of voids on shear band instabilities under plane strain conditions. *Int J Fract* 1981;17(4):389–407. <https://doi.org/10.1007/BF00036191>.
- [5] Kiran R, Khandelwal K. A triaxiality and Lode parameter dependent ductile fracture criterion. *Eng Fract Mech* 2014;128:121–38. <https://doi.org/10.1016/j.engfracmech.2014.07.010>.
- [6] Xue L. Ductile fracture modeling: theory, experimental investigation and numerical verification. PhD thesis, Massachusetts Institute of Technology; 2007.
- [7] Luo M, Wierzbicki T. Numerical failure analysis of a stretch-bending test on dual-phase steel sheets using a phenomenological fracture model. *Int J Solids Struct* 2010;47(22-23):3084–102. <https://doi.org/10.1016/j.jisolsr.2010.07.010>.
- [8] Hu Q, Li X, Han X, Chen J. A new shear and tension based ductile fracture criterion: Modeling and validation. *Eur J Mech* 2017;66:370–86. <https://doi.org/10.1016/j.euromechsol.2017.08.005>.
- [9] Quach H, Kim JJ, Nguyen DT, Kim YS. Uncoupled ductile fracture criterion considering secondary void band behaviors for failure prediction in sheet metal forming. *Int J Mech Sci* 2020;169:105297. <https://doi.org/10.1016/j.jimecsci.2019.105297>.
- [10] Park SJ, Cerik BC, Choung J. Comparative study on ductile fracture prediction of high-tensile strength marine structural steels. *Ships Offshore Struct* 2021;15(sup1):S208–19. <https://doi.org/10.1080/17445302.2020.1743552>.
- [11] Zhuang C, Mu L, Zhang J, Jiang R, Jia Z. Ductile Fracture Characterization of A36 Steel and Comparative Study of Phenomenological Models. *J Mater Civ Eng* 2021;33(1):04020421. [https://doi.org/10.1061/\(asce\)mt.1943-5533.0003543](https://doi.org/10.1061/(asce)mt.1943-5533.0003543).
- [12] Tvergaard V, Needleman A. Analysis of the cup-cone fracture in a round tensile bar. *Acta Metall* 1984;32(1):157–69. [https://doi.org/10.1016/0001-6160\(84\)90213-X](https://doi.org/10.1016/0001-6160(84)90213-X).
- [13] Gurson AL. Continuum theory of ductile rupture by void nucleation and growth: Part I—Yield criteria and flow rules for porous ductile media. *J Eng Mater Technol* 1977;99:2–15.
- [14] Andrade CMJOA. Prediction of Ductile Fracture using Uncoupled damage models. PhD thesis, University of Coimbra; 2018.
- [15] Chu CC, Needleman A. Void Nucleation Effects in Biaxially Stretched Sheets. *J Eng Mater Technol - Trans ASME* 1980;102:249–59.
- [16] Xue L. Constitutive modeling of void shearing effect in ductile fracture of porous materials. *Eng Fract Mech* 2008;75(11):3343–66. <https://doi.org/10.1016/j.engfracmech.2007.07.022>.
- [17] Lemaitre J. How to use damage mechanics. *Nucl Eng Des* 1984;80(2):233–45. [https://doi.org/10.1016/0029-5493\(84\)90169-9](https://doi.org/10.1016/0029-5493(84)90169-9).
- [18] Cao TS. Models for ductile damage and fracture prediction in cold bulk metal forming processes: a review. *Int J Mater Form* 2017;10(2):139–71. <https://doi.org/10.1007/s12289-015-1262-7>.
- [19] Xue L. Damage accumulation and fracture initiation in uncracked ductile solids subject to triaxial loading. *Int J Solids Struct* 2007;44(16):5163–81. <https://doi.org/10.1016/j.jisolsr.2006.12.026>.
- [20] Volk W, Groche P, Brosius A, Ghiotti A, Kinsey BL, Liewald M, et al. Models and modelling for process limits in metal forming. *CIRP Ann Manuf Technol* 2019;68(2):775–98.
- [21] Park S-J, Lee K, Cerik BC, Choung J. Comparative Study on Various Ductile Fracture Models for Marine Structural Steel EH36. *J Ocean Eng Technol* 2019;33(3):259–71. <https://doi.org/10.26748/ksoe.2019.038>.
- [22] Zhang XW, Wen JF, Zhang XC, Wang XG, Tu ST. Effects of the stress state on plastic deformation and ductile failure: Experiment and numerical simulation using a newly designed tension-shear specimen. *Fatigue Fract Eng Mater Struct* 2019;42(9):2079–92. <https://doi.org/10.1111/ffe.13084>.
- [23] Erice B, Roth CC, Mohr D. Stress-state and strain-rate dependent ductile fracture of dual and complex phase steel. *Mech Mater* 2018;116:11–32. <https://doi.org/10.1016/j.mechmat.2017.07.020>.

- [24] Gorji MB, Mohr D. Predicting shear fracture of aluminum 6016–T4 during deep drawing: Combining Yld-2000 plasticity with Hosford-Coulomb fracture model. *Int J Mech Sci* 2018;137:105–20. <https://doi.org/10.1016/j.ijmecsci.2018.01.008>.
- [25] Cockcroft MG, Latham DJ. Ductility and the Workability of Metals. *J Inst Metals* 1968;96:33–9.
- [26] Bai Y, Wierzbicki T. A comparative study of three groups of ductile fracture loci in the 3D space. *Eng Fract Mech* 2015;135:147–67. <https://doi.org/10.1016/j.engfractmech.2014.12.023>.
- [27] Børvik T, Dey S, Clausen AH. Perforation resistance of five different high-strength steel plates subjected to small-arms projectiles. *Int J Impact Eng* 2009;36(7):948–64. <https://doi.org/10.1016/j.ijimpeng.2008.12.003>.
- [28] Bao Y, Wierzbicki T. A comparative study on various ductile crack formation criteria. *J Eng Mater Technol* 2004;126(3):314–24. <https://doi.org/10.1115/1.1755244>.
- [29] Lou Y, Huh H, Lim S, Pack K. New ductile fracture criterion for prediction of fracture forming limit diagrams of sheet metals. *Int J Solids Struct* 2012;49(25):3605–15. <https://doi.org/10.1016/j.ijsolstr.2012.02.016>.
- [30] Li H, Fu MW, Lu J, Yang H. Ductile fracture: Experiments and computations. *Int J Plast* 2011;27(2):147–80. <https://doi.org/10.1016/j.iijplas.2010.04.001>.
- [31] Lou Y, Huh H. Extension of a shear-controlled ductile fracture model considering the stress triaxiality and the Lode parameter. *Int J Solids Struct* 2013;50(2):447–55. <https://doi.org/10.1016/j.ijsolstr.2012.10.007>.
- [32] Bai Y. Effect of Loading History on Necking and Fracture. PhD thesis, Massachusetts Institute of Technology; 2007.
- [33] Mae H, Teng X, Bai Y, Wierzbicki T. Comparison of ductile fracture properties of aluminum castings: Sand mold vs. metal mold. *Int J Solids Struct* 2008;45(5):1430–44. <https://doi.org/10.1016/j.ijsolstr.2007.10.016>.
- [34] Mae H, Teng X, Bai Y, Wierzbicki T. Ductile fracture locus of AC4CH-T6 cast aluminium alloy. *Arch Comput Mater Sci Surf Eng* 2009;1(2):100–5.
- [35] Bai Y, Wierzbicki T. A new model of metal plasticity and fracture with pressure and Lode dependence. *Int J Plast* 2008;24(6):1071–96. <https://doi.org/10.1016/j.iijplas.2007.09.004>.
- [36] Bai Y, Teng X, Wierzbicki T. On the application of stress triaxiality formula for plane strain fracture testing. *J Eng Mater Technol Trans ASME* 2009;131(2):021002. <https://doi.org/10.1115/1.3078390>.
- [37] Giglio M, Manes A, Viganò F. Ductile fracture locus of Ti-6Al-4V titanium alloy. *Int J Mech Sci* 2012;54(1):121–35. <https://doi.org/10.1016/j.ijmecsci.2011.10.003>.
- [38] Lee J, Kim SJ, Park H, Bong HJ, Kim D. Metal plasticity and ductile fracture modeling for cast aluminum alloy parts. *J Mater Process Technol* 2018;255:584–95. <https://doi.org/10.1016/j.jmatprotec.2017.12.040>.
- [39] Coulomb C. Essai sur une application des règles de maximis et minimis à quelques problèmes de statique relatifs à l'architecture. *Mem Acad Roy des Sci* 1776.
- [40] Bai Y, Wierzbicki T. Application of extended Mohr-Coulomb criterion to ductile fracture. *Int J Fract* 2010;161(1):1–20. <https://doi.org/10.1007/s10704-009-9422-8>.
- [41] Li Y, Wierzbicki T, Sutton MA, Yan J, Deng X. Mixed mode stable tearing of thin sheet Al 6061–T6 specimens: Experimental measurements and finite element simulations using a modified Mohr-Coulomb fracture criterion. *Int J Fract* 2011;168(1):53–71. <https://doi.org/10.1007/s10704-010-9554-x>.
- [42] Butcher C, Abedini A. On Phenomenological Failure Loci of Metals under Constant Stress States of Combined Tension and shear: Issue of Coaxiality and Non-Uniqueness. *Metals* 2019;9(10):1052.
- [43] Cao T-S, Gaillac A, Montmitonnet P, Bouchard PO. Identification methodology and comparison of phenomenological ductile damage models via hybrid numerical-experimental analysis of fracture experiments conducted on a zirconium alloy. *Int J Solids Struct* 2013;50(24):3984–99. <https://doi.org/10.1016/j.ijsolstr.2013.08.011>.
- [44] Li Y, Luo M, Gerlach J, Wierzbicki T. Prediction of shear-induced fracture in sheet metal forming. *J Mater Process Technol* 2010;210(14):1858–69. <https://doi.org/10.1016/j.jmatprotec.2010.06.021>.
- [45] Zhu Y, Engelhardt MD. Prediction of ductile fracture for metal alloys using a shear modified void growth model. *Eng Fract Mech* 2018;190:491–513. <https://doi.org/10.1016/j.engfractmech.2017.12.042>.
- [46] Wen H, Mahmoud H. New Model for Ductile Fracture of Metal Alloys. I: Monotonic Loading. *J Eng Mech* 2016;142(2):04015088. [https://doi.org/10.1061/\(asce\)em.1943-7889.0001009](https://doi.org/10.1061/(asce)em.1943-7889.0001009).
- [47] Papasidero J, Doquet V, Mohr D. Determination of the Effect of Stress State on the Onset of Ductile Fracture Through Tension-Torsion Experiments. *Exp Mech* 2014;54(2):137–51. <https://doi.org/10.1007/s11340-013-9788-4>.
- [48] Mohr D, Marcadet SJ. Micromechanically-motivated phenomenological Hosford-Coulomb model for predicting ductile fracture initiation at low stress triaxialities. *Int J Solids Struct* 2015;67:40–55. <https://doi.org/10.1016/j.ijsolstr.2015.02.024>.
- [49] Ha J, Baral M, Korkolis YP. Plastic anisotropy and ductile fracture of bake-hardened AA6013 aluminum sheet. *Int J Solids Struct* 2018;155:123–39. <https://doi.org/10.1016/j.ijsolstr.2018.07.015>.
- [50] Fras T, Roth CC, Mohr D. Fracture of high-strength armor steel under impact loading. *Int J Impact Eng* 2018;111:147–64. <https://doi.org/10.1016/j.ijimpeng.2017.09.009>.
- [51] Papasidero J, Doquet V, Mohr D. Ductile fracture of aluminum 2024–T351 under proportional and non-proportional multi-axial loading: Bao-Wierzbicki results revisited. *Int J Solids Struct* 2015;69:459–74.
- [52] Pack K, Marcadet SJ. Numerical failure analysis of three-point bending on martensitic hat assembly using advanced plasticity and fracture models for complex loading. *Int J Solids Struct* 2016;85:144–59. <https://doi.org/10.1016/j.ijsolstr.2016.02.014>.
- [53] Bao Y, Wierzbicki T. On the cut-off value of negative triaxiality for fracture. *Eng Fract Mech* 2005;72(7):1049–69. <https://doi.org/10.1016/j.engfractmech.2004.07.011>.
- [54] Lou Y, Yoon JW, Huh H. Modeling of shear ductile fracture considering a changeable cut-off value for stress triaxiality. *Int J Plast* 2014;54:56–80. <https://doi.org/10.1016/j.iijplas.2013.08.006>.
- [55] Lou Y, Chen L, Clausmeyer T, Tekkaya AE, Yoon JW. Modeling of ductile fracture from shear to balanced biaxial tension for sheet metals. *Int J Solids Struct* 2017;112:169–84. <https://doi.org/10.1016/j.ijsolstr.2016.11.034>.
- [56] Park N, Huh H, Lim SJ, Lou Y, Kang YS, Seo MH. Fracture-based forming limit criteria for anisotropic materials in sheet metal forming. *Int J Plast* 2017;96:1–35. <https://doi.org/10.1016/j.iijplas.2016.04.014>.
- [57] Lou Y, Yoon JW. Anisotropic ductile fracture criterion based on linear transformation. *Int J Plast* 2017;93:3–25. <https://doi.org/10.1016/j.iijplas.2017.04.008>.
- [58] Quach H, Kim JJ, Sung JH, Kim YS. A novel uncoupled ductile fracture criterion for prediction of failure in sheet metal forming. *IOP Conf Ser Mater Sci Eng* 2020;967(1):012032.
- [59] Basaran M. Stress state dependent damage modeling with a focus on the Lode angle influence. PhD thesis, RWTH Aachen University; 2011.
- [60] Ebnoether F, Mohr D. Predicting ductile fracture of low carbon steel sheets: Stress-based versus mixed stress/strain-based Mohr-Coulomb model. *Int J Solids Struct* 2013;50(7-8):1055–66. <https://doi.org/10.1016/j.ijsolstr.2012.11.026>.
- [61] Chaimongkon T, Panich S, Uthaisangsuk V. Anisotropic fracture forming limit curve and its applications for sheet metal forming with complex strain paths of aluminum sheet. *Int J Adv Manuf Technol* 2021;115(11):3553–77. <https://doi.org/10.1007/s00170-021-07357-z>.
- [62] Jia Z, Mu L, Guan B, Qian L-Y, Zang Y. Experimental and Numerical Study on Ductile Fracture Prediction of Aluminum Alloy 6016–T6 Sheets Using a Phenomenological Model. *J Mater Eng Perform* 2022;31(2):867–81.
- [63] Bharti S, Gupta A, Krishnaswamy H, Panigrahi SK, Lee MG. Evaluation of uncoupled ductile damage models for fracture prediction in incremental sheet metal forming. *CIRP J Manuf Sci Technol* 2022;37:499–517. <https://doi.org/10.1016/j.cirpj.2022.02.023>.
- [64] Cerik BC, Lee K, Park SJ, Choung J. Simulation of ship collision and grounding damage using Hosford-Coulomb fracture model for shell elements. *Ocean Eng* 2019;173:415–32. <https://doi.org/10.1016/j.oceaneng.2019.01.004>.
- [65] Kim M, Lee H, Hong S. Experimental determination of the failure surface for DP980 high-strength metal sheets considering stress triaxiality and Lode angle. *Int J Adv Manuf Technol* 2019;100(9):2775–84. <https://doi.org/10.1007/s00170-018-2867-z>.

- [66] Johnson GR, Cook WH. Fracture characteristics of three metals subjected to various strains, strain rates, temperatures and pressures. *Eng Fract Mech* 1985;21(1):31–48. [https://doi.org/10.1016/0013-7944\(85\)90052-9](https://doi.org/10.1016/0013-7944(85)90052-9).
- [67] Bao Y, Wierzbicki T. On fracture locus in the equivalent strain and stress triaxiality space. *Int J Mech Sci* 2004;46(1):81–98. <https://doi.org/10.1016/j.ijmecsci.2004.02.006>.
- [68] Teng X, Wierzbicki T. Evaluation of six fracture models in high velocity perforation. *Eng Fract Mech* 2006;73(12):1653–78. <https://doi.org/10.1016/j.engfracmech.2006.01.009>.
- [69] Asadi M, Haji Aboutalebi F, Poursina M. A comparative study of six fracture loci for DIN1623 St12 steel to predict strip tearing in a tandem cold rolling mill. *Arch Appl Mech* 2021;91(4):1859–78. <https://doi.org/10.1007/s00419-020-01859-0>.
- [70] Maclean CG. Fracture and Plasticity Characterization of DH-36 Navy Steel. PhD thesis, Massachusetts Institute of Technology; 2012.
- [71] Dunand M, Mohr D. On the predictive capabilities of the shear modified Gurson and the modified Mohr-Coulomb fracture models over a wide range of stress triaxialities and Lode angles. *J Mech Phys Solids* 2011;59(7):1374–94. <https://doi.org/10.1016/j.jmps.2011.04.006>.
- [72] Lou Y, Huh H. Evaluation of ductile fracture criteria in a general three-dimensional stress state considering the stress triaxiality and the lode parameter. *Acta Mech Solida Sin* 2013;26(6):642–58. [https://doi.org/10.1016/S0894-9166\(14\)60008-2](https://doi.org/10.1016/S0894-9166(14)60008-2).
- [73] Zhuang X, Wang T, Zhu X, Zhao Z. Calibration and application of ductile fracture criterion under non-proportional loading condition. *Eng Fract Mech* 2016;165:39–56. <https://doi.org/10.1016/j.engfracmech.2016.08.021>.
- [74] Dunand M, Mohr D. Effect of Lode parameter on plastic flow localization after proportional loading at low stress triaxialities. *J Mech Phys Solids* 2014;66:133–53. <https://doi.org/10.1016/j.jmps.2014.01.008>.
- [77] Khan AS, Liu H. A new approach for ductile fracture prediction on Al 2024–T351 alloy. *Int J Plast* 2012;35:1–12. <https://doi.org/10.1016/j.ijplas.2012.01.003>.
- [78] Vershinin VV. Validation of metal plasticity and fracture models through numerical simulation of high velocity perforation. *Int J Solids Struct* 2015;67:127–38. <https://doi.org/10.1016/j.ijsolstr.2015.04.007>.
- [79] Seidt JD. Plastic Deformation and Ductile Fracture of 2024–T351 Aluminum under Various Loading Conditions. PhD thesis, the Ohio State University; 2010.
- [80] Faleskog J, Barsoum I. Tension-torsion fracture experiments - Part I: Experiments and a procedure to evaluate the equivalent plastic strain. *Int J Solids Struct* 2013;50(25–26):4241–57. <https://doi.org/10.1016/j.ijsolstr.2013.08.029>.
- [81] Li W, Jing Y. A Simple Calibrated Ductile Fracture Model and Its Application in Failure Analysis of Steel Connections. *Buildings* 2022;12(9):1358. <https://doi.org/10.3390/buildings12091358>.
- [82] Zhuang X, Meng Y, Zhao Z. Evaluation of prediction error resulting from using average state variables in the calibration of ductile fracture criterion. *Int J Damage Mech* 2018;27(8):1231–51. <https://doi.org/10.1177/1056789517728563>.
- [83] Quach H, Kim YS. Effect of non-associated flow rule on fracture prediction of metal sheets using a novel anisotropic ductile fracture criterion. *Int J Mech Sci* 2021;195:106224. <https://doi.org/10.1016/j.ijmecsci.2020.106224>.